Radial migration of stars, measured in *N*-body simulations

Daniel Mikkola

Lund Observatory
Lund University

2017-EXA128

Degree project of 60 higher education credits (for a degree of Master)
August 2017

Supervisor: Paul McMillan

Lund Observatory
Box 43
SE-221 00 Lund
Sweden

Populärvetenskaplig beskrivning

Galaktisk arkeologi kallas det forskningsfältet inom astronomin som undersöker Vintergatans historia i termer av stjärnors kemi, ålder, utveckling, och inte minst deras kinematik. Vintergatan började som ett band av dimma över natthimlen innan människan förstod att det var våran egen Galax, som vi själva satt inuti. Sedan dess har vi försökt förstå allt vi kan om Vintergatan. Galaktisk arkeologi är forskningen om Galaxens olika komponenter, deras ursprung och deras utveckling.

Vi är dock väldigt begränsade i hur djupt in i Vintergatan vi kan se. Rymdteleskopet Hipparcos kunde upplösa objekt ner till en millibågsekund. Det motsvarar ungefär att kunna upplösa en människa på månens yta. Den nya satelliten Gaia kan nå ner till en mikrobågsekund, vilket motsvarar att upplösa en pennspets på månen. Gaia har precis börjat ge resultat dock och vi kan för tillfället inte nå längre än Solens 'kvarter' i Vintergatan.

Men även i denna begränsade sfär har vi kunnat skapa många teorier och modeller om hur stjärnor rör på sig, hur de formas och hur de utvecklas. Oftast har man börjat med de enklaste approximationerna och hur stjärnor rör sig i Galaxen är inget undantag. Den enklaste bilden är att de rör sig i nästan cirkulära banor kring Galaxens center. Men detta tillsammans med ett antagande om att den enda kemiska berikning som sker är genom stjärnors explosiva död leder till ett förutsägande att varje del av Galaxen borde utvecklas separat från de andra. Med modeller som visar att mängden metaller i stjärnor minskar desto längre ut man kommer i Vintergatan så blir varje radie unik och borde ha en rätt strikt definierad relation mellan åldern på en stjärna och dess kemiska komposition. Detta är dock inte vad vi ser.

När vi pratar kemisk komposition av en stjärna pratar vi gärna om metallicitet, som skrivs [Fe/H], och är relaterat till mängden järn gentemot väte i en stjärna. När metallicitet och ålder jämförs hade de enkla antaganden som beskrevs ovan gett en nära relation. Men observationer visar att varje ålder har en spridning i metallicitet. En av förklaringarna till detta är att stjärnor inte rör sig i nästan cirkulära banor utan kan oscillera i radie från en plats till en annan, eller till och med migrera radiellt och hamna på en helt ny plats i Galaxen. Alltså sker en hel del blandning av stjärnorna. Oscillerande radie är ett fenomen som kallas 'blurring' och radiell migrering genom interaktion med spiralarmar kallas för 'churning'. Fenomenet churning beskrevs först för galaxer av Jerry Sellwood och James Binney i en artikel år 2002. De visade också att den främsta processen för att skapa spridningen, churning, kan ske utan att lämna några dynamiska fotspår i stjärnan. Detta betyder att dess omloppsbana inte behöver bli mer elliptisk när den interagerar med en spiralarm.

För att undersöka radiell migrering använder man sig av simulering eftersom det kan ta flera hundra miljoner år. Många olika studier har genomförts men har i stor utsträckning varit begränsade i vad de tittar på för sorts galax eller hur många olika galaxer de simulerar. I detta arbete ska jag och min handledare göra en storskalig studie av hur radiell migrering är annorlunda från galax till galax genom att genomföra flera olika simuleringar. Vi kommer dessutom kolla på stjärnors vertikala egenskaper för att se vad dessa spelar för roll. Vertikala egenskaper har varit i fokus i tidigare artiklar där det varit debatt om en stjärna migrerar mindre eller ej om den är vertikalt långt ifrån galaxdisken.

Contents

Chapter 1

Introduction

The purpose of Galactic archaeology is determining the history of the Milky Way (MW) Galaxy. To do this one uses observational data from stellar populations in terms of properties such as kinematics, chemistry, ages, and evolution. In this context a population means stars with similar characteristics and the most notable population is "the Solar Neighbourhood" (SN). Stars orbit with a 'guiding radius' defined as $R_{\rm g} \sim L_z/V_{\rm c}$ where L_z is the angular momentum in z-direction (perpendicular to the disc of the Galaxy) and $V_{\rm c}$ the circular velocity in the potential. If we make the two assumptions that **(1)** stars do not significantly change their radius over time and **(2)** the Galactic disc is axisymmetric, we can view populations like the SN as representative samples of the history of the Galaxy at their given radius. With these assumptions the content at one radius is isolated, so using it to make assumptions about the past history for a certain radius is a powerful approach.

If the assumptions hold true, we can use the age-metallicity relation (AMR) and the metallicity distribution function (MDF) of stars to find out the entire history of the MW disc at a given radius. The metallicity of stars and interstellar medium (ISM) should increase with time as metals are created predominantly in supernovae, so newer stars are more metal rich. Thus, we can predict that metallicity decreases with age. Considering only this, we expect the distribution of stellar metallicity to have a peak. This is because fewer very metal-poor stars should be left alive and conversely not so many very metal-rich stars have been born so far as have in the peak. However with basic modelling of this kind the "G-dwarf problem" arises in which the number of metal-poor stars are too many compared to observations (Searle & Sargent 1972). A proposed solution revolves around gas in- and outflow (Larson 1974). In such a suggestion it is recognised that different regions of the Galaxy are not isolated and can undergo mixing. Also, more recent observations (e.g. Holmberg et al. 2009) suggest that the observed AMR is flat and has a large scatter in metallicity at a given age.

Kinematic properties of stars can usually tell us a lot about stars. Stars move in various ways and can have eccentric orbits in which case they can spend some time on radii different from their present one. The eccentricity of a star's orbit can be identified from the velocity of the star at different times. This might tells us that the star has had a dynamical interaction with something in the past. Instead consider the more devious case where a star's orbital radius is changed while the orbit remains as circular as before. It would end up in a region with different typical metallicity content while having a metallicity indicative of its own birthplace. We would be unable to identify a kinematic difference between this star and one that has been born and remained in the same region throughout its lifetime in contrast to the eccentric star.

The first idea of a process of diffusion through the disc comes from Wielen (1977) but only regards diffusion through interaction with giant molecular clouds (GMCs) which is insufficient at changing the radius of stars enough for mixing. Two ways of changing the radius of a star are called blurring and churning. The former, blurring, is when stars have non-circular orbits. No star has a truly circular orbit, but the degree to which they are eccentric varies. Because of the eccentric motion stars trace out what is called epicyclic orbits and visit radii up to a kiloparsec different than their mean radial distance. Coupled with the fact that observations show clear radial metallicity gradients in the disc (e.g. Vila-Costas & Edmunds 1992; de Jong 1996) it is clear that this effect would cause chemical mixing in the Galaxy.

Regarding churning, it was shown in a paper by Sellwood & Binney (2002) that resonant interaction with spiral arms in the Galaxy should be taken into account as well and is in fact the principal driver of what we call radial migration. Churning is also a process which arises naturally within the Galactic disc if there are spiral arms and can move stars across much greater distances than blurring and does it without changing the star's eccentricity, leaving no dynamical trace of occurrence.

The Milky Way has complicated structure and content with different populations, thick and thin discs, flaring, a halo, and more (Bland-Hawthorn & Gerhard 2016) and not everything observed in these parts is explainable or likely due to radial migration. But behaviour involving more than one part of the disc can be investigated to ascertain if radial migration is part of the solution. A feature long noted in the Milky Way is the existence of, as stated above, two separate discs, the thin and the thick discs. We can identify their differences through properties such as velocity dispersion, metallicities, and ages with some small overlap (Haywood 2008).

There has been explanations beyond radial migration given to account for differences between the discs (see e.g. Chiappini et al. 1997; Bensby et al. 2005) but the duality of the discs is one of the cases where radial migration offers a solution. Schönrich & Binney (2009) performed simulations of Galactic chemical evolution and included radial mixing. They were able to produce a thick and thin disc from radial migration and showed that it can be used to explain some of the observations found in the Galaxy.

Over recent years, a large number of numerical simulations of Galaxies with radial migration have been performed and analysed (see e.g. Sellwood & Binney 2002; Solway et al. 2012; Roškar et al. 2012; Vera-Ciro et al. 2014; Halle et al. 2015). A good example of other more comprehensive studies is a series of papers lead by Michael Aumer and James Binney (Aumer et al. 2016a,b; Aumer & Binney 2017; Aumer et al. 2017) where they perform a large N-body study of galaxies with live dark matter halos and include the effects of combined spirals/bar and GMCs. They study the growth and evolution of thick and thin discs under different conditions. Studies such as these have increased the understanding of radial migration which is a topic still not completely understood. This is where the work of this thesis comes into play.

The work presented in this thesis differs from those previously stated in that they have mostly focused on individual, or in other ways somewhat limited, simulations while this work is intended to have a broad scope of investigation. A large number of different N-body simulations have been performed where different initial conditions have been used. By investigating the positions and

velocities of the stars the radial migration of each simulation can be gauged. The nature of radial migration depends strongly on the conditions of the galaxy in which it transpires. The effect of conditions that will be investigated are the varying halo mass, the subsequent effect on spiral arms in terms of strength and quantity, the stability of the disc in terms of dynamics, and the robustness to numerical alterations regarding number of bodies, duration, and seed numbers. This will provide a greater understanding of radial migration and provide a basis for future work in analytical models or other N-body simulations.

Chapter 2

Theory

2.1 Observational background

A galaxy is a mixture of stars, gas, and dark matter (DM). The stars are the source of most activity in a galaxy, the constituents of stellar groups, clusters, the origin of supernovae and so on, and in between them is the ISM and dark matter. If we observe stars at different radii we find a radial metallicity gradient (Hayden et al. 2015). The stars are responsible for the metallicity content of a region due to the production of elements in their cores. They burn through fusion and create more massive elements which they then eject back out into the ISM through their deaths. Larger stars undergo supernovae and deposit elements not found through big bang nucleosynthesis. Normally metallicity is quantified through the difference of the logarithmic ratio of iron to hydrogen to that of the Sun. This is written

$$[\mathrm{Fe/H}] = \log\left(\frac{N_{\mathrm{Fe}}}{N_{\mathrm{H}}}\right)_{\mathrm{star}} - \log\left(\frac{N_{\mathrm{Fe}}}{N_{\mathrm{H}}}\right)_{\odot}, \tag{2.1}$$

where N stands for the number of atoms of each kind. Assuming that a region stays relatively isolated we would expect a region to increase in metallicity over time. So looking at ages and metallicities one could naively expect a decline in metallicity as the age of stars in a region increases, see e.g. Bensby et al. (2014) or Bergemann et al. (2014). In the former paper, they derived abundances for 714 F and G dwarfs and subgiant stars in the Solar neighbourhood. The result for [Fe/H] against age is shown in figure 2.1.

The age-metallicity relation (AMR) in figure 2.1, does not appear to have the predicted behaviour. At a given metallicity there are a range of available ages with a large scatter. A similar plot can be found in Bergemann et al. (2014). The same behaviour can be seen there and the AMR almost appears to be flat. Radial migration is a solution that naturally occurs in the presence of spiral arms and which could produce the result we see. Stars can move to regions with very different metallicity than where they started.

Looking at more specific abundances, we briefly outline the three primary sites of stellar nucleosynthesis as discussed by Edvardsson et al. (1993):

(i) Stars of large mass ($M > 8M_{\odot}$), contribute as dominant source of O and α-elements (O, Ne, Mg, etc).They start to create onion-like shells of different materials as they fuse all the way up to the iron peak. Stellar winds drive some of this material back to the surroundings but

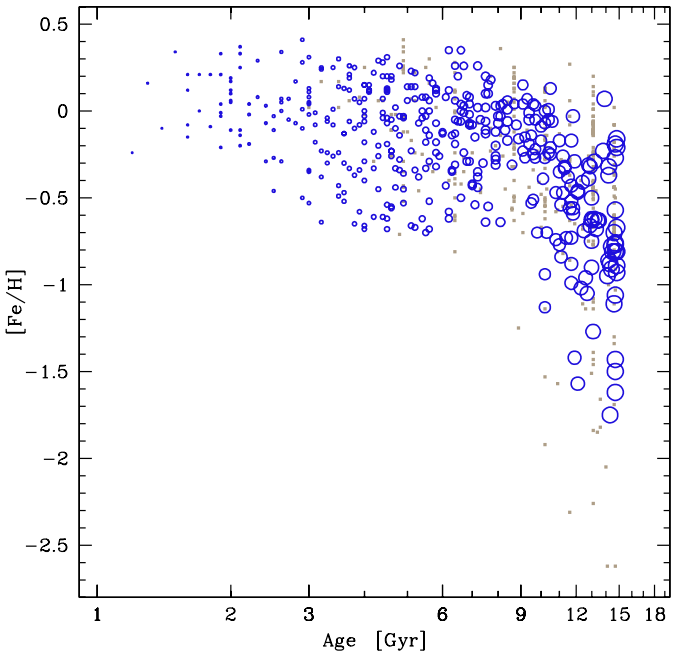

Figure 2.1: Figure 2Ia from Bensby et al. (2014). It shows metallicity against age in Gyr. Blue circles are stars with an age difference between upper and lower estimates below 4 Gyr and the size increases with age. The grey dots are stars with bigger uncertainties.

the main driver is the core-collapse supernova which ends the life of the star. This is a type II supernova.

(ii) A white dwarf that accretes mass can become a type Ia supernova. They create elements in a process called thermal runaway fusion which creates mostly iron peak elements such as iron and nickel. White dwarfs are born of stars of lower mass, below $8M_{\odot}$ (although most of the contribution is from 1-3$M_{\odot}$ stars).

(iii) The same stars that form white dwarfs in (ii) will in a past period in their lives be asymptotic giant branch stars (AGB stars) which can create heavy elements through what is called the s-process (slow process). They produce elements such as Y, Zr, Ba, and Nd. Stellar winds and eventually superwinds that result in planetary nebulae return these elements to the ISM.

But the way these various processes come into being have vastly different time-scales. Massive stars, responsible for the production of α-elements, cause (i) and require some tens of millions of years to occur. Even heavier stars are faster. This is because the lifetime of a star is shorter with mass as the burning proceeds faster. Less massive stars, which cause (ii) and (iii), take billions of years. The expected lifetime of the Sun is 10 billion years. In that time, a couple of hundred of massive stellar lifetimes will have passed. Meaning that process (i) will have transpired long before (ii) starts. For the case of this study, case (iii) is less important as we care more for the amount of alpha-elements and iron in the Galaxy.

Fuhrmann (2011) analysed the abundances of over 300 nearby solar-type stars which allows us to investigate the relative abundances of α-elements and iron. Schönrich & Binney (2009) modelled chemical evolution of the SN by selecting stars from their model which resembled stars from the Geneva-Copenhagen survey of the SN (Nordström et al. 2004).

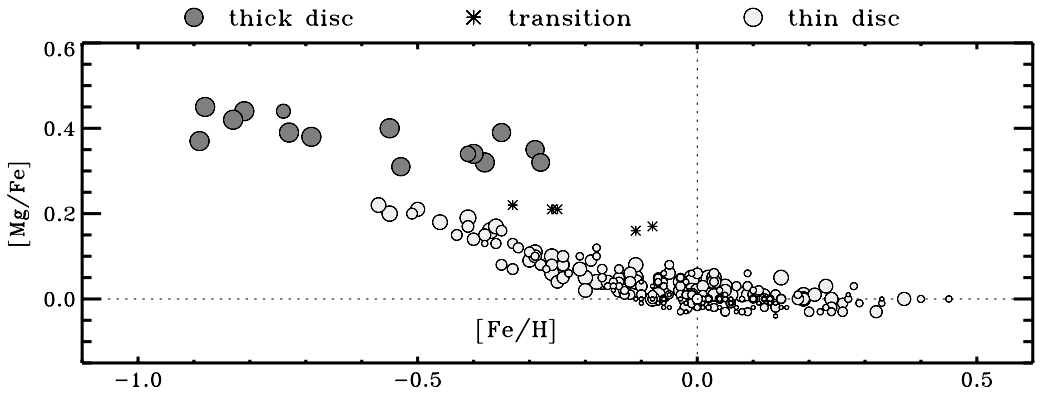

Figure 2.2: Figure 15 from Fuhrmann (2011). [Mg/Fe] against metallicity for over 300 SN stars. The figure shows different discs using different symbols as explained through the figure. The size of circles are in proportion to the determined ages.

If we turn to figure 2.2 we notice a separation that is quite clearly labelled in this plot. The thick and thin discs vary in metallicity and, although not shown here, in velocity dispersion. The chemical evolution we predicted can broadly be seen. First we have type II supernovae which over time would provide a roughly constant amount of [α/Fe]. But hydrogen is not produced, so [Fe/H] increases to the right. Eventually type Ia supernovae begin and the iron increases faster than the α-elements, leading to a decline.

There are different gradients of metallicity in the Galaxy. Hayden et al. (2015) found a decrease in [Fe/H] with galactocentric radius for low altitudes above the disc. Higher up above the disc, [Fe/H] is generally lower but does not change much at all with radius. Essentially the vertical gradients disappear closer to the edge of the Galaxy. For [α/Fe], the distributions in metallicity are quite similar, but at larger distances from the midplane of the Galaxy, the inner disc has slightly higher [α/Fe] and somewhat more of a gradient than does [Fe/H] in the same regions. To summarise there are negative gradients for [Fe/H] with radius near the disc and less so above it and gradients with vertical distance, z, in the inner disc. [α/Fe] show similar gradients but with a radial gradient also at higher z.

Following the above, we could view the x-axis of figure 2.2 as some indication of radius within a population and the y-axis very roughly as age. When type Ia supernovae then begin, a transition down to the thin disc would occur. The number of stars between the discs would depend on the duration of the transition. In this picture we would then see, chemically, the evolution of the ISM in a region of the Galaxy as a line through the data with no width to it. Since these are all local stars, the width of the populations implies mixing as lines of other regions would be shifted to the left and right. A separation is also observed rather than a smooth transition between the thick and thin discs. Solutions that have been given to explain this behaviour are: a break in the star formation history (Chiappini et al. 1997) and accretion events (Bensby et al. 2005).

In Schönrich & Binney (2009) they provide a similar plot with O instead of Mg. In that paper they extend models to include radial migration and achieve similar results. They reproduce the dichotomy of figure 2.2. But more importantly, they show that the stars at the SN do deviate from

the path of the ISM in the [α/Fe]/[Fe/H] space. The extent of the deviation is larger than what would be expected of blurring alone which is a further indication of radial migration as churning. In plots like figure 2.2 the stars do not follow a line defined by the ISM either which suggests that radial migration is apparent in the Milky Way. Indeed, the result from Sellwood & Binney (2002) is that if transient spiral arms are present radial migration *will* occur.

2.2 Computational background

The force that is most relevant on astrophysical distance scales is gravity. When objects are very far apart but of very large masses it is the only contributing force. Astronomers and physicists since Newton have strived to describe, as accurately as possible, the motions of celestial bodies. Following from Newton's law of gravitation every body in a system experiences an acceleration due to the gravitational attraction of all other present bodies which leads to the following description of acceleration

$$\frac{d^2x_i}{dt^2} = -\sum_{j=1;\ j\neq i}^{N} \frac{Gm_j(x_i - x_j)}{|x_i - x_j|^3}, \tag{2.2}$$

for a system of N bodies with masses m_j. G is the gravitational constant and j and i are the indices of two bodies. This is a second order differential equation which has seen analytical solutions for a handful of bodies. It becomes a matter of increasing complexity when N rises higher and analytical solutions are abandoned in favour of numerical ones. This gives rise to the subject of N-body modelling.

In N-body simulations N can rise to very higher numbers. However it is necessary to specify a divide between the type of systems simulated. The *relaxation time* is defined as the time after which cumulative kicks from other bodies have significantly altered a bodies orbit. It is given as (Binney & Tremaine 2008)

$$t_{\rm relax} \simeq \frac{0.1N}{\ln N} t_{\rm cross}, \tag{2.3}$$

with $t_{\rm cross}$ being the time it takes for a body to cross the system once which in galaxy simulations is the time it takes for a star to cross the galaxy. When studying dynamics below $t_{\rm relax}$ the collisions are not important and we call them collisionless systems. To give an example from Binney & Tremaine (2008) galaxies typically have 10^{11} stars and are a few hundred crossing times old. They would need to be around half a billion crossing times old before reaching the relaxation time. For clusters however relaxation can strongly influence the structure over its lifetime. In 2011 collisionless simulations could reach over 10^9 bodies while collisional ones only 10^6 (Dehnen & Read 2011) due to the complexity of handling collisions.

Within these two categories there are plenty of examples of how N-body simulations are applicable in astrophysics. Planet formation (O'Brien et al. 2006), Planetary dynamics (Mustill et al. 2017), stellar cluster dynamical evolution (Hurley et al. 2007), and galaxy formation (Agertz & Kravtsov 2016) are just a few examples. More applications outside of astrophysics exist as well but will not be mentioned here. We will instead focus on simulations of disc galaxies.

The last decade or so has seen plenty of galaxy simulations which have given rise to the study of radial migration. The seminal paper of the field is by Sellwood & Binney (2002). They utilised a particle-mesh (PM) method to study N-body radial migration. PM has since been replaced by

P3M, or the particle-particle-particle-mesh method. In their paper they showed the effect of radial migration with a single and controlled spiral arm. Schönrich & Binney (2009), although not using N-body simulations, investigated the chemical evolution with radial migration by expanding on a model from Roškar et al. (2008b) which uses `GASOLINE` (Wadsley et al. 2004), a smoothed particle hydrodynamics (SPH) code with N-body integration. which allows it to also follow gas dynamics. They were able to produce thick and thin discs and performed comparison with observational data. Solway et al. (2012) ran a number of simulations using a 3D polar grid-based code which is outlined in Sellwood & Valluri (1997). From their simulations they stated findings that migrators are vertically colder stars. The opposite was found by Vera-Ciro et al. (2014) which used the code `GADGET-2` (Springel 2005) which is a parallel TreeSPH code.

There are a number of topics on which the effect of different dynamical evolution scenarios can be studied. We previously mentioned work by Aumer & Binney (Aumer et al. 2016a,b; Aumer & Binney 2017; Aumer et al. 2017) where they use combinations of spirals/bar and GMC effects as well as different thick disc formation scenarios to match results with the Milky Way. They find that in their models, migration alone is unable to produce a thick disc (Aumer et al. 2016b). Work by Ivan Minchev (Minchev et al. 2015, 2014) also look into the formation of thick discs in simulations as well as the role of radial migration during the formation of galaxies rather than in formed galaxies such as those appearing in this study.

These simulations are typically performed with one or two important restrictions. First they are often performed in a controlled manner with strong induced spiral arms, see e.g. Sellwood & Binney (2002) or Solway et al. (2012). Secondly they can be focused on a single simulation from which results are deduced, see e.g. Vera-Ciro et al. (2014), Halle et al. (2015), or Kawata et al. (2017). In this work I will try to address both of these limitations by running a very large number of simulations that vary a lot from one to the other as well as having the features of the simulation arise naturally without being induced. Some of the aims of this work is to be able to describe how the results change depending on the simulation that is performed and to get a better grip on the concept of radial migration as well as provide understanding of some discrepancies that appear in the literature.

2.3 Blurring

Two different sources for radial migration exist in galaxies and both are important for understanding the observable structure of any galaxy. The two processes related to the orbits of stars are called *blurring* and *churning*. We will start with the former.

Stars start on nearly circular orbits with small variations. These nearly circular orbits do not send the star onto very different radii. Stars can however undergo scattering events with heavier and larger features like giant molecular clouds (GMCs). By dynamically scattering, these stars can be moved onto slightly eccentric orbits. Small radial oscillations in a star's orbit are treated by the *epicycle approximation* and hence these orbits are called epicyclic orbits. An example of how this can look is given in figure 2.3. In the figure the star moves interior and exterior to the circular orbit by some 1-2 kpc, so chemical mixing between different parts of the Galaxy by blurring is most likely occurring.

We shall now consider non-circular motions that can occur in the plane of a galaxy. For simplicity,

the forces are specific forces. We can express a central gravitational force in terms of the rotational velocity $V_c(R)$ as

$$F_g(R) = \frac{V_c(R)^2}{R}, \tag{2.4}$$

where R is the distance from the center of the galaxy and indices c and g are for circular and gravity respectively. Standard cases of F_g are exterior to a spherical mass, $F_g \propto R^{-2}$, and the inside of a homogeneous sphere, $F_g \propto R$. We can also tell that a constant V_c yields $F_g \propto R^{-1}$. We summarize with

$$F_g = F_0 \left(\frac{R}{R_0}\right)^{\alpha} \tag{2.5}$$

where α can be between -2 and 1. If α is less than -2 it implies a negative mass density in Poisson's equation. F_0 denotes the force at the Sun's distance which is R_0. The value of α near the Sun can be determined using local parameters.

We give the force near the sun as $F_0 = v_0^2/R_0$, where v_0 is the circular velocity of the Sun. With angular momentum $L_0 = v_0 R_0$ we can write $F_0 = L_0^2/R^{-3}$. The angular velocity is $\omega_0 = v_0/R_0$. Angular velocity and angular momentum are constant for a circular orbit. This means that the star will not move radially from R_0, the equilibrium distance because the gravitational force will balance the centrifugal force.

Instead we now consider a non-circular orbit where the radius will change over time. Gravitational force can still be expressed with equation (2.4):

$$F_g(R) = \frac{V_c(R)^2}{R} = \left(\frac{R}{R_0}\right)^{\alpha} \frac{L_0^2}{R_0^3}, \tag{2.6}$$

While the centrifugal force is expressed

$$F_c = \omega^2 R. \tag{2.7}$$

Because the angular velocity is not constant we replace ω with $\omega = L_0/R^2$ and write

$$F_c(R) = L_0^2 R^{-3}. \tag{2.8}$$

We can now ponder a situation in which a star on a circular orbit receives a small boost in the outward radial direction. As the star begins to move outward equations (2.6) and (2.8) govern the force changes. The former changes as R^{α} and the other as R^{-3}. Since α must be greater than -2, the centrifugal force decreases more rapidly and the star accelerates back radially inwards. In the situation in which the boost is towards the centre the centrifugal force will increase faster and the star will accelerate outward again. Therefore the motion of the star is stable to small velocity changes and would instead start to produce radial oscillations. This causes what is called an *epicyclic* orbit.

The motions in the epicycle orbit are approximated by harmonic oscillators with the solutions

$$\begin{aligned} \xi(t) =& a \sin(\kappa t + \varphi) \\ \eta(t) =& \frac{2\omega_0}{\kappa} a \cos(\kappa t + \varphi), \end{aligned} \tag{2.9}$$

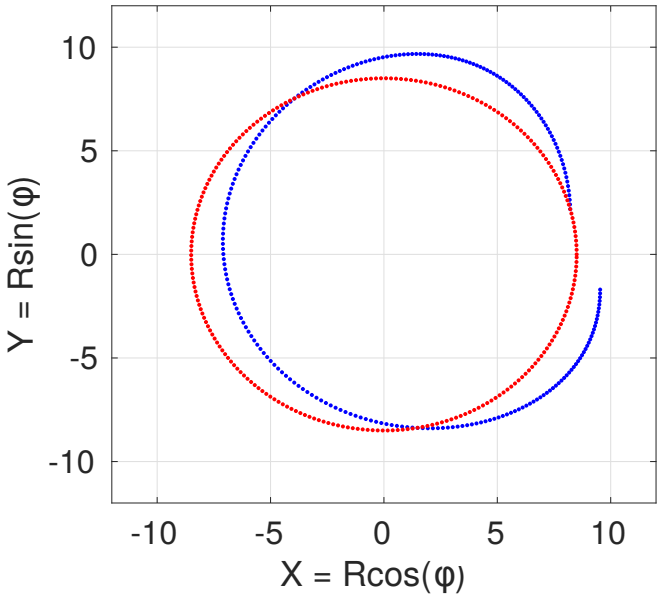

Figure 2.3: An epicyclic orbit (blue) and a circular orbit (red) plotted for ~ 240 Myr with $\kappa = 35.3$ km/s/kpc, $A = 14$,$B = -12$ km/s/kpc, $a = 1.5$ kpc, and $R_0 = 8.5$ kpc as the guiding radius.

Here $\xi(t)$ is an approximation of the radial motion, $\eta(t)$ describes the part of the azimuthal motion which is non-circular, a and φ are the amplitude and phase respectively κ is the *epicycle frequency* which is given through the expression

$$\kappa(R_g) = \sqrt{\left(R\frac{d\Omega^2}{dR} + 4\Omega^2\right)_{R_g}}, \tag{2.10}$$

where Ω is the circular frequency of the orbit and R_g the guiding radius the epicycle orbit oscillates about. The frequency κ can be simplified with the inclusion of two new functions, A and B,

$$A(R) \equiv \frac{1}{2}R\frac{d\Omega}{dR} \tag{2.11}$$

$$B(R) \equiv -\left(\Omega + \frac{1}{2}R\frac{d\Omega}{dR}\right), \tag{2.12}$$

called **Oort's** constants which are measurable. With A and B, κ simplifies to $\sqrt{-4B(A-B)}$ or $\omega_0\sqrt{(3+\alpha)}$. The ratio of amplitude between $\xi(t)$ and $\eta(t)$ is then

$$\frac{2\omega_0}{\kappa} = \frac{2}{\sqrt{3+\alpha}} = \sqrt{\frac{A-B}{-B}}, \tag{2.13}$$

which, using literature values of A and B, becomes 1.47. For a full and thorough derivation of this, see Binney & Tremaine (2008). This result means that the epicycles are 'dragged out' in the azimuthal direction. To illustrate this I plot an epicyclic orbit against a circular one in figure 2.3. The circular orbit is marked in red and the epicyclic one in blue.

So stars have epicycle orbits and thus perform radial excursion. By putting blurring in the

concept of chemical mixing in the Galaxy, we can convince ourselves of its relevance with ease as it occurs over a few million years. Stars move onto radii different than their guiding radius and are then capable of enriching other regions of the Galaxy. In fact, the guiding radius itself can be changed by interactions that produce the kick necessary for epicyclic orbits. The Galactic disc is dynamically heated over time (Wielen 1977) from various overdensities like GMCs which are able to produce the kick.

The metallicity broadening that comes from blurring is not enough to explain observations from the Geneva-Copenhagen survey (Nordström et al. 2004) however and accounts for only up to 50% of the observed scatter in metallicity that can be seen in plots like figures 2.1 and 2.2 (Schönrich & Binney 2009; Roškar et al. 2008a).

2.4 Churning

Another contributor to radial migration and the most important one is angular momentum transfer via scattering by spiral arms. This is called *churning* and we will now explain this phenomena.

In order to explain the process of churning in a simple manner we will use an extremely simplified picture of a star near the co-rotation velocity of a single spiral arm which does not change through the evolution of its host galaxy.

Let us start by defining the torque. The torque is the cross product of a force vector, $\boldsymbol{F}$, and a positional vector, $\boldsymbol{r}$.

$$\boldsymbol{\Gamma} = \boldsymbol{r} \times \boldsymbol{F}. \tag{2.14}$$

Angular momentum is the cross product of the position and momentum, $\boldsymbol{p}$,

$$\boldsymbol{L} = \boldsymbol{r} \times \boldsymbol{p} \tag{2.15}$$

and thus changes as

$$\dot{\boldsymbol{L}} = \frac{d}{dt}(\boldsymbol{r} \times \boldsymbol{p}) = (\dot{\boldsymbol{r}} \times \boldsymbol{p}) + (\boldsymbol{r} \times \dot{\boldsymbol{p}}). \tag{2.16}$$

Since $\boldsymbol{p} = m\dot{\boldsymbol{r}}$ and $\dot{\boldsymbol{p}} = m\ddot{\boldsymbol{r}} = \boldsymbol{F}$, the first parenthesis equals zero and the second remains as

$$\dot{\boldsymbol{L}} = \boldsymbol{r} \times \boldsymbol{F} = \boldsymbol{\Gamma}. \tag{2.17}$$

So the torque describes the change of angular momentum. The magnitude is less of importance than the sign. The magnitude of the angular momentum is proportional to the radius and the circular velocity. The process we are now going to describe is illustrated in figure 2.4. Here a single spiral arm is marked out. Corotation is marked out with a dotted line which means that at this radius stars orbit with the same pattern speed as the spiral arm. Interior to this stars move faster and exterior they move slower relative to the spiral arm in terms of angular velocity.

We start with the star moving slower than the spiral arm. It is the red dot to the top left in the illustration. It is moving slower than the arm so in the rotating frame appears to be moving towards the spiral arm. The force points to the right and the position points outwards and hence the torque is negative. A negative torque, according to equation (2.17), means that the angular momentum decreases and the radius then decreases and the star ends up on an orbit interior to the

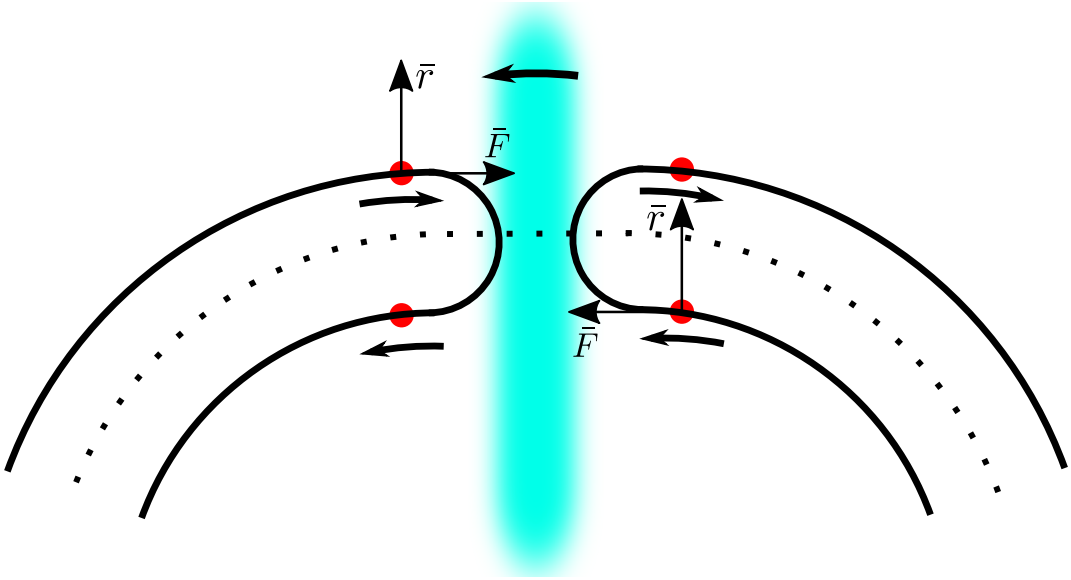

Figure 2.4: An illustration of the principle of angular momentum transfer at corotation. Red dots mark different positions in time for the horseshoe orbit of the star and the spiral arm is in teal. The dotted line marks the radius of corotation. The vectors of force and position are indicated as well as direction of rotation of the spiral arm.

arm. Now it will orbit faster and appear to move away from the spiral arm which is the lower left red dot. It comes around and catches up to the spiral arm in the red dot on the lower right. The force now points in the other direction and thus the torque is positive, the star gains angular momentum and moves to an exterior radius. The net effect of this interaction is zero. However, spiral arms are not fixed features of a galaxy. They are transient objects and multiple spiral arms usually exist. Hence by the time the star interacts with a spiral arm a second time, the spiral arm will be different and so will the interaction with it. So when a more complicated scenario is considered the net effect is unlikely to be zero and radial migration can happen both inwards and outwards in a galaxy.

This was shown more rigorously in Sellwood & Binney (2002) where spiral arms caused churning of stars and gas while retaining overall angular momentum distribution and with very little increase in random motion. In their paper they start at the *Jacobi integral* (for a description and derivation see appendix A, the experienced reader can skip this.) $E_\mathrm{j} = E - \Omega_p L$, where $E = H$, the Hamiltonian, since this Hamiltonian is equal to the total energy E. The Jacobi integral is constant in time so the change between two moments in time yields the equation

$$\Delta E = \Omega_p \Delta L. \tag{2.18}$$

But we can also describe the change in energy in parts. The radial and azimuthal kinetic energy can approximate the energy change through the equation

$$\Delta E = \frac{\partial H}{\partial L}\Delta L + \frac{\partial H}{\partial J_R}\Delta J_R, \tag{2.19}$$

which is the differential of the Hamiltonian under the assumption that it only depends on L and J_R, that is, we treat the system as 2D. We have introduced the variable J_R, called radial action. To understand it we must briefly cover **angle-action variables**. These variables are, in a sense, a

different set of coordinates. One way to illustrate this is in figure 2.5. Here the action is the area of one of the rings and the angle is indicated in the figure. Angle-actions coordinates are not identical, but closely analogous, to polar coordinates in this manner.

Now recall Hamiltonian mechanics and Hamilton's equations,

$$\dot{\mathbf{q}} = \frac{\partial H}{\partial \mathbf{p}} \quad , \quad \dot{\mathbf{p}} = -\frac{\partial H}{\partial \mathbf{q}}. \tag{2.20}$$

We wish to describe the Hamiltonian using the angle-action variables with our momenta being the actions **J** and coordinate θ. The actions are assumed integrals of motion and therefore

$$\dot{J}_i = -\frac{\partial H}{\partial \theta_i} = 0. \tag{2.21}$$

Which then leads to the derivative of the coordinate

$$\dot{\theta}_i = \frac{\partial H}{\partial J_i} = \Omega_i(\mathbf{J}), \tag{2.22}$$

an angular frequency. With this knowledge, returning to equation (2.19), we can find the solution to the partial derivatives. With radial action and angular momentum, we get $\partial H/\partial L = \Omega$ and $\partial H/\partial J_R = \omega_R$, the azimuthal and radial frequencies respectively. The equation now looks like

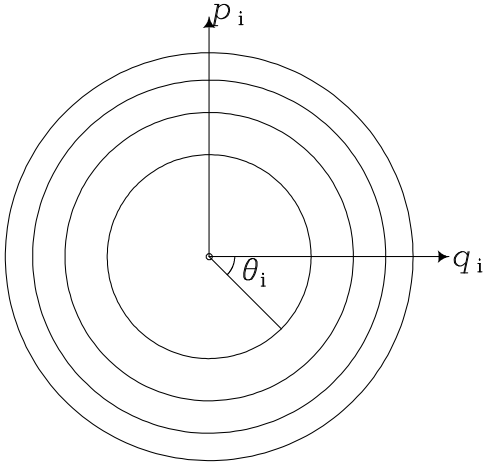

Figure 2.5: Figure from page 214 of Binney & Tremaine (2008) illustrating the concept of angle-action variables as similar to polar coordinates. The momentum p_i and coordinate q_i are given as the area of the rings, called the action J_i, and the angle θ_i.

$$\Delta E = \Omega \Delta L + \omega_R \Delta J_R. \tag{2.23}$$

Putting this in equation (2.18) gives

$$\Delta J_R = \frac{\Omega_p - \Omega}{\omega_R} \Delta L. \tag{2.24}$$

Which means that a change in angular momentum changes the radial action unless changes in angular momentum occur at corotation ($\Omega = \Omega_p$). A change in the radial action would mean that a star would change its eccentricity.

Actions are very useful units to have. They have already been discussed as area to position and momentum coordinates but what they quantify are oscillations. The radial action is an expression of the radial oscillations and the vertical action, J_z, an expression of the vertical oscillations. They are able to combine different properties with, for example, J_z being a combination of v_z and z. As actions are a combination of other variables and conserved in the approximation they simplify interpretation of the results. The actions are conserved quantities as they are assumed integrals of motion.

The fact that radial action does not change for angular momentum changes at corotation is one of the perhaps more frustrating features of churning. While it is the stronger out of blurring and churning, it also occurs at corotation without leaving behind a dynamical trace. This makes

deducing trends and population behaviour from observations much more troublesome because not only do we have methods for moving stars from different parts of a galaxy to another but churning dynamically hides itself. To emphasise this, some papers suggest that the Sun itself came from a radius ~ 2 kpc closer in than where it is today (Wielen et al. 1996).

It cannot be said that radial migration is the sole solution for the observed behaviour in the Galaxy. It is likely to be occurring however and may well be a contributor along with other proposed methods to create the observed chemical mixing. Since radial migration is a process that occurs over very large timescales the way to study it is in computer simulations which can then be run for billions of years with millions of particles. With the inclusions of chemical evolution models for the Galaxy it is possible to attempt to generate observables or to simply probe the nature of these process and what affects them.

Radial migration is not a completely understood mechanism and there exists several important questions, one of which is which stars that undergo migration. It is unclear if gradients in migration exist in properties such as radius, height above the disc, or dynamical temperature. A simple picture can be painted from the theory which is that stars that are dynamically cold, or spends more of their time close to the midplane of the disc, would have a greater opportunity to participate in churning by the spiral arms. This would put constraints of both the height above the disc and the dynamical temperature. The literature on this subject is not clear and an answer to this question is important as galaxies have vertical metallicity gradients so it would be useful to know what part of the disc should be taken into account, as it would have an effect on the observed spread in metallicities.

The strength of a spiral arm can be expected to have a relation with the amount of radial migration that occurs. The number of spiral arms that form and their strength is not fully understood either and more importantly what determines it. Results have shown a relation between the number of spiral arms that are formed with respect to disc to DM halo ratios and radius (D'Onghia 2015). There might be relationships between the strength and the number of spiral arms that form. This is an important question when it comes to future analytical modelling within the field. Analytical models rely on the results provided in simulations and the behaviour they display.

These questions regarding which stars are migrating, what their properties are and what types of discs it occurs in, what spiral arms form and at what strengths, will be further addressed in sections 4.1 and 4.2.

Chapter 3

Methods

3.1 Simulations

The simulations are run with packages that exist within Peter Teuben's NEMO toolbox (Teuben 1995 `https://bima.astro.umd.edu/nemo/`). For a list of parameters used in the packages with explanations, please see appendix B.

3.1.1 Initial conditions: `mkWD99disc`

The disc

The disc in my simulations is created in the way described in McMillan & Dehnen (2007). It is designed to ensure that the disc begins in equilibrium. We will go through the method briefly here.

To start, an approximation is made that the motion of all particles in the disc is separated into planar and vertical parts with energies that are separately conserved. These parts are given as

$$E_{\parallel} \equiv \frac{1}{2}(v_R^2 + v_\phi^2) + \Phi(R, 0) \tag{3.1}$$

$$E_{\perp} \equiv \frac{1}{2}v_z^2 + \Phi(R, z) - \Phi(R, 0). \tag{3.2}$$

It turns out that for orbits close to the disc, $|z| \ll R$, this approximation is excellent. The three velocities are described in cylindrical coordinates and the potential Φ is the total potential of the system (disc model + halo). The disc model potential is found from Dehnen & Binney (1998) and the halo from Dehnen & McLaughlin (2005).

To obtain the distribution function (DF) which informs us of how our positions and velocities of the particles are distributed, we follow the approach laid out by Dehnen (1999). First observe the simplest DF, a dynamically cold disc with all particles on circular orbits. With disc density $\rho = \Sigma(R)\delta(z)$ Dehnen (1999) expresses this

$$f_{\rm cold}(E_{\parallel}, L_z, z, v_z) = \frac{\Omega(R_{L_z})\Sigma(R_{L_z})}{\pi\kappa(R_{L_z})}\delta[E_{\parallel} - E_{\rm c}(R_{L_z})]\delta(z)\delta(v_z), \tag{3.3}$$

where $\Sigma(R)$, $\kappa(R)$ are angular and epicycle frequencies at radius R. $E_{\rm c}(R)$ is energy of a circular orbit. R_{L_z} is the radius of an orbit with z-component angular momentum L_z. The δ-functions are

replaceable by exponentials if one wants to achieve a warm disc DF.

In the same paper Dehnen argues that it is better to use an alternative form for the cold disc,

$$f_{\rm cold}(E_\parallel, L_z, z, v_z) = \frac{\Omega(R_{E_\parallel})\Sigma(R_{E_\parallel})}{\pi\kappa(R_{E_\parallel})}\delta\Omega(E_\parallel)[L_z - L_{\rm c}(R_{E_\parallel})]\delta(z)\delta(v_z). \tag{3.4}$$

Here $R_{E_\parallel}$ is the radius of a circular orbit with energy $E_\parallel$. We warm the disc up by replacing the delta functions with exponentials. We arrive at the rather long expression

$$f_{\rm disc}(E_\parallel, E_\perp, L_z) = \frac{\Omega(R_{E_\parallel})\tilde{\Sigma}(R_{E_\parallel})}{(2\pi)^{3/2}\kappa(R_{E_\parallel})}\frac{1}{z_d\sigma_z(R_{E_\parallel})}\exp\left[-\frac{E_\perp}{\sigma_z^2(R_{E_\parallel})}\right] \times \frac{1}{\tilde{\sigma}_R^2(R_{E_\parallel})}\exp\left(\frac{\Omega(R_{E_\parallel})[L_z - L_{\rm c}(R_{E_\parallel})]}{\tilde{\sigma}_R^2(R_{E_\parallel})}\right). \tag{3.5}$$

The new parameters $\tilde{\Sigma}(R)$ and $\tilde{\sigma}_R(R)$ are sought such that the true surface density and radial velocity dispersion profiles in the N-body system match whichever is desired. Following exercise 4.21 of Binney & Tremaine (2008) which assumes an axisymmetric and isothermal disc, we arrive at a velocity dispersion in the vertical direction of $\sigma_z^2(R) = \pi G z_d \Sigma(R)$ for a given radius where z_d is the scale height of the disc. The reason Dehnen (1999) argues for this DF is that $R_{E_\parallel}$ better approximates the mean radius of a given orbit than R_{L_z} which also means that $\Sigma(R)$ and $\sigma_R(R)$ more closely resemble the heated DF counterparts $\tilde{\Sigma}(R)$ and $\tilde{\sigma}_R(R)$.

The sampling of the DF is performed so as to minimize noise. To this end we sample orbits from the density distribution $\tilde{\Sigma}(R)$ and place $1 \ll N_{\rm sam} \ll N_{\rm disc}$ particles on points of each orbit. The parameters $\tilde{\Sigma}(R)$ and $\tilde{\sigma}_R(R)$ are then iteratively adapted so that the actual surface density and velocity dispersion match the desired ones as well as possible. The disc is truncated at five scale radii to concentrate particles in the main area of the disc.

The halo

The halo model we have used is given in Dehnen & McLaughlin (2005) and is added onto the disc. They find, for the enclosed mass profile and density, the equations

$$M(r) = M_{\rm tot}\left(\frac{x^{4/9}}{1+x^{4/9}}\right)^5 \tag{3.6}$$

$$\rho(r) = \frac{5}{9}\frac{M_{\rm tot}}{\pi r_0^3}x^{-7/9}(1+x^{4/9})^{-6}, \tag{3.7}$$

Where $x \equiv r/r_0$ and r_0 is the scale radius. $M_{\rm tot}$ is the total halo mass. From integration of $GM(r)/r^2$ the gravitational potential can also be found

$$\Phi(r) = -\frac{9}{4}\frac{GM_{\rm tot}}{r_0}B_{\frac{1}{1+x^{4/9}}}\left(\frac{9}{4}, \frac{11}{4}\right). \tag{3.8}$$

In this equation $B_u(p,q) \equiv \int_0^u t^{p-1}(1-t)^{q-1}$ is what is called the incomplete beta function (Press et al. 1992).

Through `mkWD99disc` it is possible to select from a number of halo models by changing the `accname, accpars,` and `accfile` settings. Through parameters in `accpars` which give the inner and outer slopes of the density as well as a transition exponent the halo is determined.

3.1.2 Integration: `gyrfalcON`

The simulation is integrated using the package `gyrfalcON` which is written and developed by Walter Dehnen, in the early 00's. The full description of the algorithm is available in Dehnen (2000) and Dehnen (2002). We will provide some background of the integrator and briefly outline its unique features in the following paragraphs.

The brunt of the computational effort of N-body simulations in stellar dynamics comes from the calculation of the gravitational forces between mutually interacting bodies, which is required at each time step. This means that, most often, the error of the simulations is chiefly determined by the noise from the distribution of the simulated bodies. To avoid calculating the forces by direct summation, since it would be an exhausting task, one can instead utilise approximations which allow for greater number of particles and, hence, less noise.

A milestone for the computation of stellar dynamics came with the Barnes and Hut tree code (Barnes & Hut 1986). It is an approximate method which sorts bodies into a hierarchical tree of cubic cells. It then computes multipole moments of said cells. Once this is done, the force at the position of a body generated by the contents of a cell is calculated using a multipole expansion. The complexity then becomes $\mathcal{O}(N \log(N))$ since the number of interactions is $\mathcal{O}(\log(N))$. Here N is the number of bodies.

Apart from the tree code of Barnes and Hut, the so-called fast multipole method (FMM) has also achieved popularity. Developed by Greengard and Rokhlin (Greengard & Rokhlin 1987, 1997), FMM has a different usage and is most often designed for high accuracy which is not as important in collisionless stellar dynamics. This algorithm sorts bodies into a hierarchy of nested grids and then calculates the multipole moments of different cells and then calculates the forces between grid cells using an expansion of the multipoles. This uses spherical harmonics and cells are both sources and sinks. This reduces the complexity to $\mathcal{O}(N)$.

The idea of `gyrfalcON` is to combine the powerful tools of the tree code and FMM into a new code which is designed for low-accuracy application. It uses a hierarchical tree of cubic cells like the tree code. Mutual cell-cell interaction are utilised for force calculation where cells are sources and sinks at the same time. By keeping both nodes of an interaction as source and sink, Newton's third law is exactly conserved by construction. The code also has complexity $\mathcal{O}(N)$ but is faster than both FMM and the tree code. One of the ways the code reduces computation time is that it determines if a cell-cell interaction can be executed or must be split with an improved multipole-acceptance criterion, further outlined in Dehnen (2002).

The simulations I run are collisionless and thus do not require very high accuracy. The design of `gyrfalcON` is to suit the type of large simulations I perform here and thus it stands as a superb choice of integrator for my investigations.

Table 3.1: Time unit for various simulations.

Time conversion unit	
Simulation	Time unit in Myr
$Q = 1.5, M_{\rm h} = 12\ M_{\rm d}$	10
$Q = 1.5, M_{\rm h} = 24\ M_{\rm d}$	11
$Q = 1.5, M_{\rm h} = 36\ M_{\rm d}$	12
$Q = 1.5, M_{\rm h} = 48\ M_{\rm d}$	13
$Q = 1.5, M_{\rm h} = 60\ M_{\rm d}$	15
$Q = 1.5, M_{\rm h} = 72\ M_{\rm d}$	15
$Q = 1.2, M_{\rm h} = 24\ M_{\rm d}$	11
$Q = 3, M_{\rm h} = 24\ M_{\rm d}$	11
$N_{\rm bodies} = 2 \cdot 10^6$	11
$N_{\rm bodies} = 10^7$	11
$R_\sigma = 2$	11

3.1.3 Units and simulations

The output from the simulation comes in "code" units where $G = M_{\rm d} = R_{\rm d} = 1$. The units we use in our results are mass, length, time, or some combination of the three. The distances are in units of scale radius. This I take to be the scale radius of the Milky Way. Since this number is not well determined (Bland-Hawthorn & Gerhard 2016), I choose a number roughly in the middle of estimates, 3 kpc. The mass is in units of the total disc mass which for the Milky Way I take to be $M_d = 5 \cdot 10^{10} M_\odot$ (Bland-Hawthorn & Gerhard 2016).

The last unit, time, is more difficult to find a conversion coefficient for. This is because the unit changes between simulations. To determine the time unit I compare the acceleration felt by a region near the Sun's position in my own galaxy to that of the real Sun's acceleration towards the Milky Way centre. This can be found by the equation of centripetal acceleration and by using the proper motion of Sgr A* (Reid & Brunthaler 2004). However we perform simulations with different halo masses and as such the unit will vary. In table 3.1 the result can be seen for various simulations. Unless otherwise stated $M_{\rm h} = 24 M_{\rm d}, Q = 1.5, N_{\rm bodies} = 10^6$. This is my 'standard' simulation.

To present the results in a more understandable manner the results are given in real units (km, kpc, Gyr, $M_\odot$, etc...). To be able to do this while having a varying time unit I take the most prominent result of $t = 11$ Myr as the conversion factor for all results. This of course affects the results to some level and therefore table 3.1 is given so that a proper conversion can be performed if the reader should feel encouraged to do so.

From table 3.1 it is also evident that the parameter Q has been changed between simulations, this parameter is known as Toomre's Q or Toomre's stability criterion. It relates to the gravitational stability of differentially rotating discs and was derived for a disc of stars in Toomre (1964). For a stellar disc it is

$$Q \equiv \frac{\sigma_R \kappa}{3.36 G \Sigma} > 1, \tag{3.9}$$

where σ_R radial velocity dispersion, G is the gravitational constant, and Σ is the surface density. Toomre's Q can be thought of in the context of hot and cold discs. A dynamically hot disc will

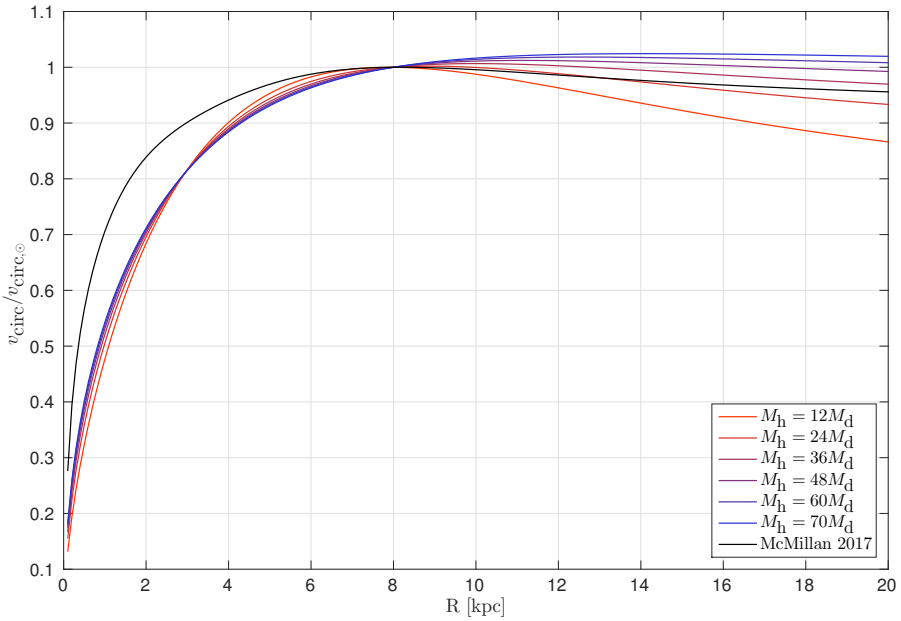

Figure 3.1: Circular velocity curves for the different halo mass simulations as well as a rotational curve from McMillan (2017) which models the Milky Way. Since the different simulations have been given the same time unit, the circular velocity is normalised to the circular velocity at $R = 8$ kpc. The curve most similar to the MW of McMillan (2017) is the 24 $M_{\rm d}$ halo simulation.

have a larger σ_R and thus a larger Q. A truly cold disc has zero velocity dispersion and zero Q. When Q is below one a wavelength exists for which the wave-equation describing the distribution of stars can grow exponentially, causing an instability. Thus we always have $Q > 1$. The higher Q is set in the simulations the more stable the disc should become.

One parameter is seen in table 3.1 which is different from the rest, namely R_σ. This parameter relates to Q and determines whether Q varies with radius. When this parameter is zero, which it is in all other simulations, Q is fixed. Otherwise the parameter determines radial velocity dispersion through

$$\sigma_R \propto \exp\left(-\frac{R}{R_\sigma}\right), \tag{3.10}$$

with the normalisation defined in such a way that $Q = 1.5$ at $R = R_{\rm d}$.

I also change the halo mass in the simulations. This is more thoroughly covered in section 4.2 but it will be briefly touched upon in a different light here. Changing the surrounding mass to an orbiting particle will have an effect on its circular velocity. This can be clearly seen in figure 3.1 where rotation curves for all halo mass simulations are shown along with that of the Milky Way from McMillan (2017). The one which behaves most similar to the Milky Way is the 24 $M_{\rm d}$ simulation. The halo mass will not only affect the circular velocities however but also the stability of the system and the strength and prevalence of spiral arms that occur. In the inner regions there is a large difference between the Milky Way rotation curve and the ones from this work which is due to the lack of a bulge in the simulations.

The halo mass is varied because of the effect it is expected to have on the spiral structure. A galaxy disc with a very heavy halo is expected to have a harder time generating strong spiral arms due to the gravitational force of the dark matter. With a lot of dark matter, the individual parts of a galaxy do not feel the influence of one another as strongly and do not merge into large spiral arms. Conversely a lighter halo is expected to be able to create fewer stronger spirals as the different parts of the disc are able to interact more strongly. This expectation is shown to occur in results like D'Onghia (2015). Not only will different halo masses allow investigation of what type of spirals and their strength that arises but also by extension show what amount of migration is linked to what type of spirals.

3.2 Analysis tools

In the following sections I will outline the methods I have used and developed. The results produced from these tools are seen in chapter 4. For a cursory reading, these sections may be skipped.

Once the output of the simulations has been produced, it needs to be analysed. To do this, I convert it from `.nemo` format to ASCII using a converter called `s2a`, made by Walter Dehnen. Once in ASCII format I have created multiple analysis tools ready to utilise. I developed these in MATLAB and will introduce them in the following subsections.

3.2.1 Radius over time

One of the more straight-forward tools I have developed is one which investigates the development of radius (measured as distance from the centre of the galaxy) over time for the top migrating particles in the simulation.

To do this the top migrators must first be deduced from the simulation. In suitable steps in time, perhaps a fifth of the total duration or smaller if the simulation runs longer, the absolute change in angular momentum is evaluated. This is specific angular momentum in the z-direction which relates to a change in the planar position of a particles.

$$L_z = x \cdot v_y - y \cdot v_x. \tag{3.11}$$

This property is investigated for each individual particle. For the next time-step it is evaluated again and the absolute angular momentum differences are added up. By then performing a filter for particles located between radii $(0-3), (3-6), (6-9), (9-12), (12-15)$ kpc respectively, I identify the indices of the particles with the maximum total difference in angular momentum. These are the top migrators in each radial bin.

The radius of the top migrators can then be extracted at every time step of the simulation and the path of radius over time can be plotted which an example of can be seen figure 4.5. By looking at the top migrators the very extremes of migration in the different simulations can be gauged as well as give a very quick and easy way to determine whether or not migration is occurring in the simulation. If even the top migrators have not changed their orbit by much the rest of the simulation is not going to show much migration.

3.2.2 Radial velocity dispersion

Another check I perform to ensure that things are behaving correctly is to investigate the radial velocity dispersion within the disc. This is simply the standard deviation of the velocities in the radial direction.

The radial velocity is calculated as the composite of the x and y velocities just as radius is with positions. To attain the standard deviation as a function of radius, $\sigma_R(R)$, a moving standard deviation through radius is calculated with a window size of $N = 10^4$ points. A moving standard deviation means that at a given point p, the closest N points are used together with p_i to calculate the standard deviation. Moving onto the next point p_{i+1} the closest N points to p_{i+1} is used. The process is repeated for all points in the series. This is then evaluated at various times of the simulation with suitable intervals. The result can be seen in figure 4.18 and is discussed in section 4.4.1.

By performing this analysis I can determine whether or not the velocity dispersion of the particles is increased over time or not. From Sellwood & Binney (2002) it is not expected that there will be a significant increase in non-circular motion.

3.2.3 ΔL_z over initial L_z

L_z is a good marker of radial migration as it will not change during blurring but only during churning or other dynamical effects. I show the change of angular momentum between initial time and after 2.2 Gyr, ΔL_z, plotted against initial L_z in the plots shown in figure 4.6. This will give an overview of which particles are migrating. However, as the number of particles in the simulation can, at times, be several millions, I also bin the particles. Creating bins in both directions gives a 90x220 sized two-dimensional bin for L_z against ΔL_z. I take care to remove empty bins and store the number of points in each bin to be able to generate a number density colour map as well.

This is a way of identifying which parts of the disc is migrating. But plotting the angular momentum in this fashion can also give indication of spiral arms which show up as diagonal regions of overdensity with a negative slope with initial angular momentum. This slope arises from churning. If a star is exactly at corotation it will not migrate as it never encounters the spiral arm. This would put it at $\Delta L_z = 0$. If the star is interior to the spiral arm, it will migrate outwards meaning that at lower L_z than corotation a positive ΔL_z is expected. Outside corotation the star is migrated inwards and would have a negative ΔL_z. So spiral arms appear as diagonal lines in these plots. This also shows how spiral arms are indeed the primary source of radial migration.

3.2.4 v_z, L_z, $\sigma_{\Delta L_z}$

My main investigations lie with determining whether or not the velocity of stars in the z-direction is of any importance. The literature has been indecisive on this issue with papers like Vera-Ciro et al. (2014) claiming the velocity matters while Solway et al. (2012) are surprised to find only very minor difference in changes in angular momentum between thick and thin discs. As such it is a suitable investigation to undertake.

L_z has already been calculated and v_z is one of the output parameters. These parameters are

taken at their initial values. Once more I perform two-dimensional binning. The size is 50x50 from 0 to the maximum of L_z. Within each bin ΔL_z is calculated and then the standard deviation is evaluated. This means that a large standard deviation corresponds to a scatter in ΔL_z and therefore migration. The standard deviation is given as a colour scheme. The result can be seen in figure 4.20 and discussed in section 4.4.2.

3.2.5 Slope of $\sigma_{\Delta L_z}$ against v_z

In the previous analysis method I wanted to see whether or not the trend existed for the whole disc. But another method I also used was to take slices in L_z at 0.2, 0.4, 0.6, and 0.8 of the maximum L_z, which corresponds to fractions of 0.2, 0.4, 0.6, and 0.8 of the maximum radius, 15 kpc. This means roughly 3, 6, 9, and 12 kpc respectively. At these slices I plot $\sigma_{\Delta L_z}$ and v_z. This way I can look for the strength of the slope to see how strong the trend is between different parts of the disc, if a trend does exist.

This is done in a very similar fashion to section 3.2.4 with binning in v_z for the given slice of L_z. We take slices of L_z for different parts of the disc to give information of the whole disc. Since the plotted points now utilise vastly different amounts of data points for the calculation of $\sigma_{\Delta L_z}$ we add a colour to each point indicative of the number of data points contained in the calculation. The result of this is seen in figures 4.8 through 4.13.

3.2.6 Fourier spectrum

If spiral arms arise it is important to determine their characteristics such as strength and frequency. To calculate these I created a routine for performing a Fourier analysis of the density of the disc to identify apparent frequencies. To do this snapshots of the data are required at much closer interval. We use a step of $\Delta t = 1$, compared to other snapshots taken at $\Delta t > 25$ depending on the simulation. A more in-depth description of the method which I have used is available in Press et al. (1992). I will briefly explain it here.

What I want is to calculate Fourier coefficients for separate frequencies, radii, and modes. The surface density of the disc can be expanded into a Fourier series given by

$$\Sigma(r, \phi) = \sum_{m=0}^{\infty} c_m(r) e^{[-im\phi_m(r)]}, \tag{3.12}$$

Here m stands for the mode or pattern multiplicity. The angle $\phi_m(r)$ is the phase of the m-th mode at a given radius r. The complex coefficient for a given radius and mode is

$$c_m(r) = \frac{1}{M(r)} \sum_{j=1}^{N} m_j e^{im\phi_j}, \tag{3.13}$$

with j as particle index. The mass of a particle is m_j and its angle between current position and x-axis is ϕ_j. N is the total number of particles within the radial bin considered. Since my particles all have the same mass, m_j can be taken out of the sum and when divided over $M(r)$ it simply becomes $1/N$.

The coefficients $c_m(r)$ are calculated once for each output of data that I have and as such are a

time series upon which a discrete Fourier transform is performed.

$$C_{k,m}(r) = \sum_{j=1}^{S-1} c_j(r,m) w_j e^{2\pi i j k/S}, \qquad k = 0, \ldots, S-1. \tag{3.14}$$

Here S is the number of time samples we have, so j now stands for an output rather than an individual particle. The index k is for separate frequencies and w_j is the window function I use which is

$$w_j(x) = e^{-(x-S/2)^2/(S/4)^2}. \tag{3.15}$$

In the window function, x is the current snapshot.

The frequency sampling is set by the length under investigation, S, and by the step between the different samples, Δt. It is

$$\Omega_k = 2\pi \frac{k}{S\Delta t} m, \qquad k = 0, 1, \ldots, S/2, \tag{3.16}$$

which then avoids some high-frequency spectral leakage. We avoid mirrored spectra at the Nyquist frequency since $\Omega_{\mathrm{Ny}} = \Omega_{S/2}$. With these tools the power spectrum can be constructed.

$$P(\Omega_k, r) = \frac{1}{W}\left[|C_k(r)|^2 + |C_{S-k}(r)|^2\right], \qquad k = 1, 2, \ldots, \frac{S}{2} - 1. \tag{3.17}$$

Here W is a normalization factor calculated as $W = \Sigma_{j=0}^{S}$. With P, Ω_k, and r it is possible to construct a contour plot to show the power spectrum. This will identify changes in the density which I assume come from phase rather than changing amplitudes.

To perform a sanity check, a fake disc is generated consisting of particles placed with a normal distribution in radius and uniform distribution in angle. Superimposed on top of this are smaller density regions following a sinusoidal wave going along the x-axis. By applying a rotation matrix to all particles belonging to the sinusoidal feature it can be caused to rotate with the desired pattern speed, which should then be identified in the Fourier power spectrum. After performing this test I confirm that pattern speeds are identified at the correct mode.

3.2.7 Wave strength

It is important to not only identify whether or not spiral arms arise but also when they do and how strong they are. To this end I find the amplitude of the waves which is given as

$$A_m(r) = |c_m(r)|. \tag{3.18}$$

I then find the maximum value of the mode and divide it by the zeroth mode amplitude. In the zeroth mode the exponentials of equation (3.12) and equation (3.13) equal one and left is the mean density of the disc. For every step in time I take $\max(A_m/A_0)$ which shows the evolution over time.

3.2.8 Metallicity distribution

Despite the simulations being rather limited in not including the effects of GMC scattering, stellar evolution, chemical enrichment, and more, including metallicity and chemistry to a small extent can still add a stronger connection to observations from my simulations. Since the simulations do not include any chemistry to begin with it needs to be added. However there is a problem in the use of modern observational values for the chemistry and is is that they represent the Milky Way *today*. It could be argued as a poor choice for initial conditions but modern values will be used regardless as they represent a reasonable gradient that could be expected for a galaxy. The results can then be used to observe instead the level and type of mixing that occurs rather than try to accurately reproduce MW values. In this way it becomes a useful indication for chemical mixing from radial migration.

For the purpose of adding metallicities the results of Hayden et al. (2015) are used. This data utilises 69,919 red giants from the APOGEE which is a spectroscopic survey which has determined chemical abundances for roughly 200,000 stars. The data is used calculate regional metallicities and metallicity gradients in the SN. (Hayden et al. 2015) provides average metallicities for regions between 3 kpc and 15 kpc, with a bin with of 2 kpc. By taking this data I fit for the gradient and extrapolate to $R = 0$. The fit that I arrive at is

$$[\mathrm{Fe/H}] = -0.0449 \cdot R + 0.334. \tag{3.19}$$

However, stars of various heights above the midplane of the disc have different gradients as well as displayed in Hayden et al. (2015). To emulate this, I use vertical action, J_z, in an additional term in the slope described above. Action is used rather than v_z or z. This is because a star that migrates inwards will reach lower z with the same v_z due to the increased density of inner regions. Moving outwards will take a star to larger z with the same v_z. At the same time the velocity v_z is affected. But between the two, J_z is roughly conserved and more useful as a gradient for the whole disc. The vertical action is described further in sections 2.4 and 4.2. The vertical action is not directly proportional to vertical height however and the following approximation is used

$$z_{\max} \approx A \frac{J_z}{\exp\left(-\frac{R}{2R_\mathrm{d}}\right)}, \tag{3.20}$$

where R_d is the scale radius and A is a constant determined through rough minimization to be (1/83). With this, the new gradient is

$$[\mathrm{Fe/H}] = -0.0449 \cdot R + 0.334 - \frac{1}{83} \frac{J_z}{\exp\left(-\frac{R}{2R_\mathrm{d}}\right)} \tag{3.21}$$

I use equation (3.21) with initial radius for R to 'paint' the stars in the simulation with metallicity. Then at the end of the simulation three metallicity distributions are produced by selecting stars that are within the Solar neighbourhood equivalent of the simulation ($7.5 < R < 8.5$) kpc and dividing them into three vertical regions of $J_z < 5$ kpc km s^{-1}, $5 \leq J_z < 15$ kpc km s^{-1}, and $15 \leq J_z$ kpc km s^{-1}.

Chapter 4

Results

4.1 Spiral formation and radial migration

The formation of spiral arms is a central part of my work and therefore the results of a set of simulations will now be presented in this context. The focus here will be on showing the different type of spirals that arise in various simulations and the gauge what effect this has upon the migration that transpired within that disc. A set of simulations with different halo masses are selected for review in this context and they are further described in section 4.2.

The difference in appearance between a light and heavy DM halo is shown in figures 4.1 and 4.2 which are snapshots of their respective disc at halfway through and at the end of the simulations. The exact masses are 12 M_{d} and 72 M_{d} for the DM halos to give the largest visual difference available.

The differences between a heavy halo and a light halo has striking differences when the galaxy is viewed face-on. We can see that the low mass halo simulation shows a significant growth in radial extent with only a few defined, strong spiral arms as well as what appears to be a bar-like feature. This is in strong contrast to the heavy halo mass disc which which does not grow radially, with many spiral-like features that are rather weak. Neither does a bar form.

To gain an overview of the spirals that form in terms of angular frequency, radial extent, and duration, the Fourier spectrum described in section 3.2.6 is used on a part of the disc between 3-9 kpc. It is limited to this region to avoid two things. 1) The influence of a bar-like feature, and 2) misidentification of noise in the outer regions. These are two features that can occur during the analysis which will hide any spiral features in the Fourier spectrum. The complement to this analysis is that I also use the method in 3.2.7 to see the amplitude ratios which is what provides information about when and how long the spiral features exist.

The results of these analysis tools are given in figures 4.3 and 4.4. The results are presented for the simulations with DM halo mass 12 M_{d}, 24 M_{d}, 48 M_{d}, and 72 M_{d} from left to right in the figures. These four simulations are selected as they have an appropriate range of masses. In each simulation, seven different modes are shown. It might appear that, at first glance of figure 4.3, there are spirals appearing at multiple modes and across all simulations. There are a few things to remember when viewing this figure. In each respective plot, the maximum power is shown regardless of the other plots for the same simulation. Also if a spiral has shown up during any point in the simulation it will appear and spirals from different times can be identified simultaneously. These two

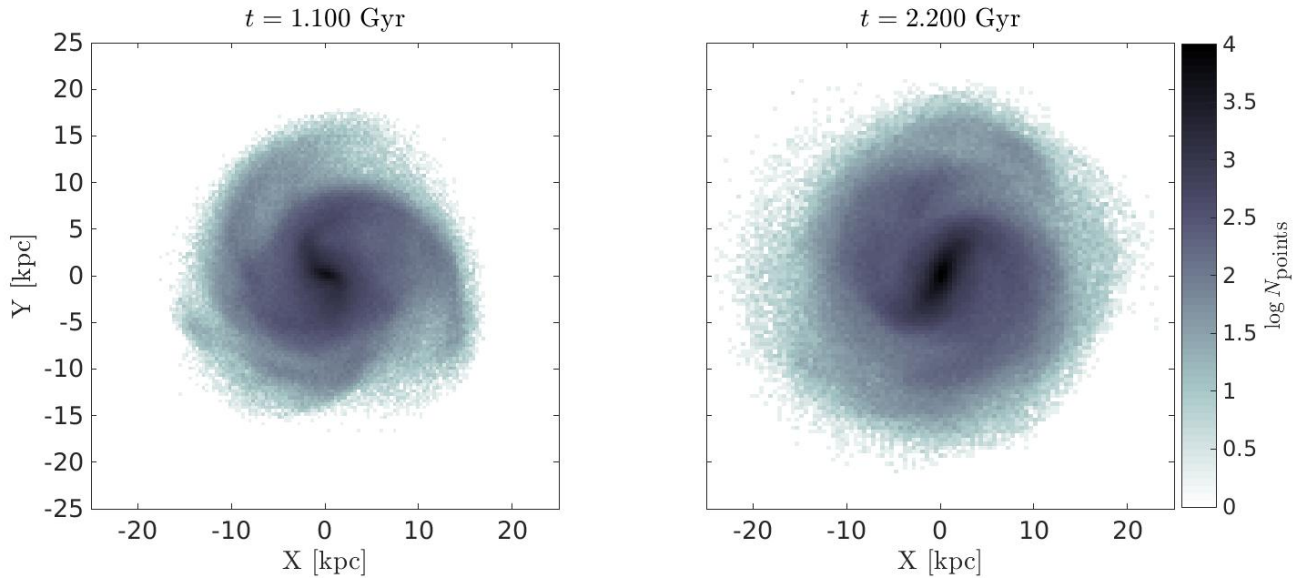

Figure 4.1: The 12 M_{d} halo mass simulation galaxy viewed face-on at 1.1 Gyr into the simulation on the left and at the end of the simulation, 2.2 Gyr, on the right. The points here are from 100x100 2D bins in X and Y. The colour gives the logarithm of the number of particles within a bin. Only a few, strong spiral arms appear.

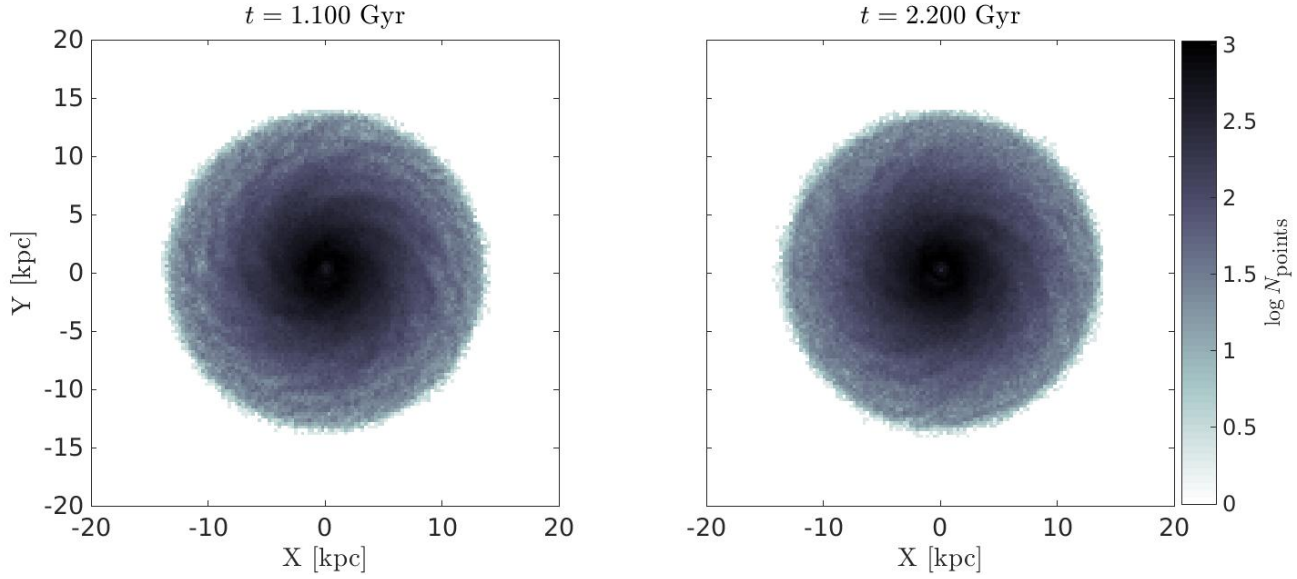

Figure 4.2: The particle density of the simulation with a 72 M_{d} halo, comparable to figure 4.1 of a different simulation. The spiral arms appear considerably weaker and more numerous with a heavier halo.

figures are best viewed side-by-side as figure 4.4 shows both the strength of a spiral and when it arises.

It becomes evident from viewing these plots that as the simulations begin spiral arms do eventually arise. The actual strength of the spiral arms are smaller for the heavier halo mass simulations. This is expected as spirals can grow more easily in a disc-dominated galaxy as was discussed in sections 2.4 and 3.1.3.

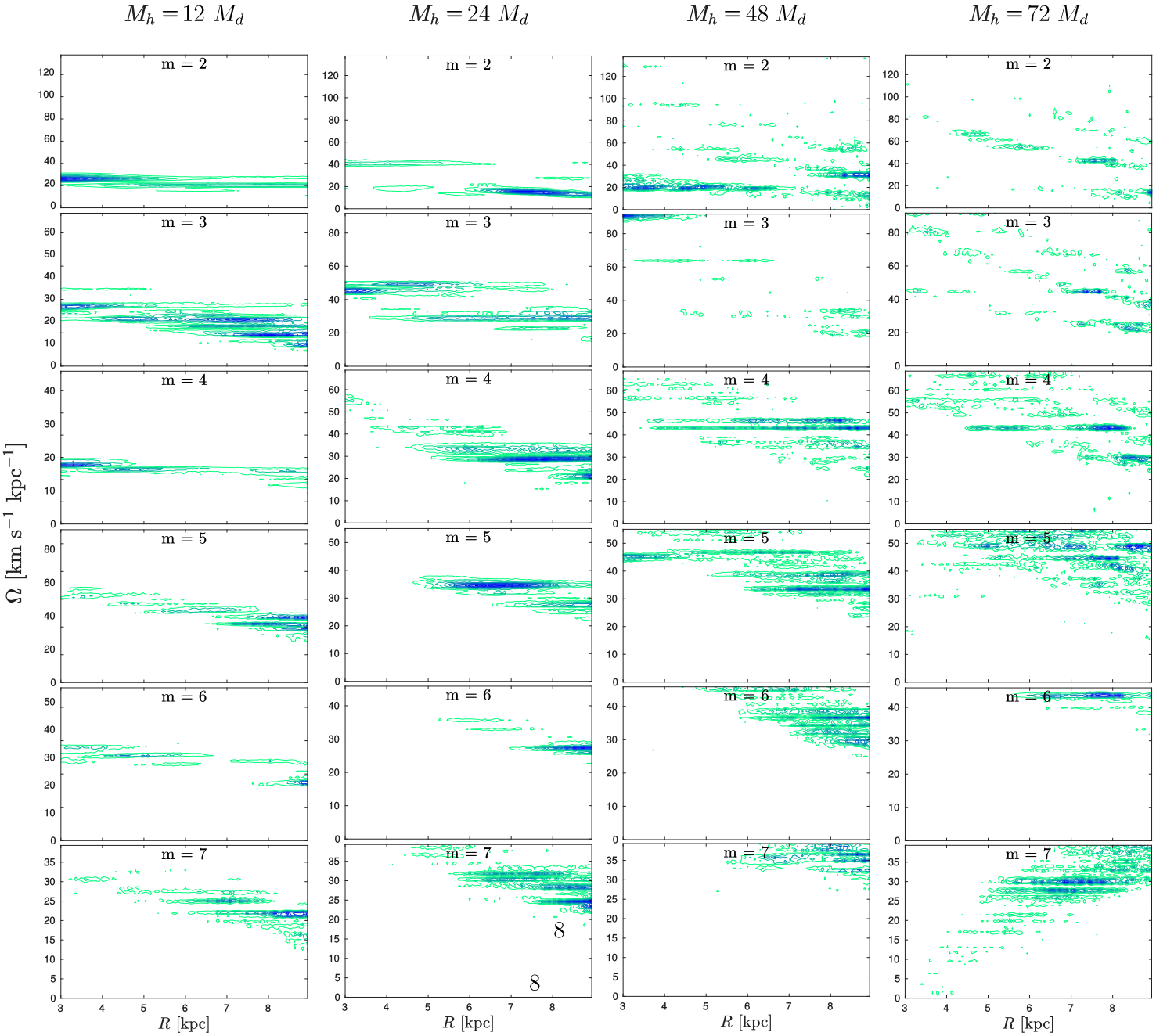

Figure 4.3: Fourier spectrum of four different simulations given in four columns. The simulations are 12 $M_{\rm d}$, 24 $M_{\rm d}$, 48 $M_{\rm d}$, and 72 $M_{\rm d}$ from left to right. The axes show radius and angular frequency. Each row shows a mode ranging from 2 to 7. Moving from top left to bottom right increases the number of detected patterns, indicating that individual spirals become weaker.

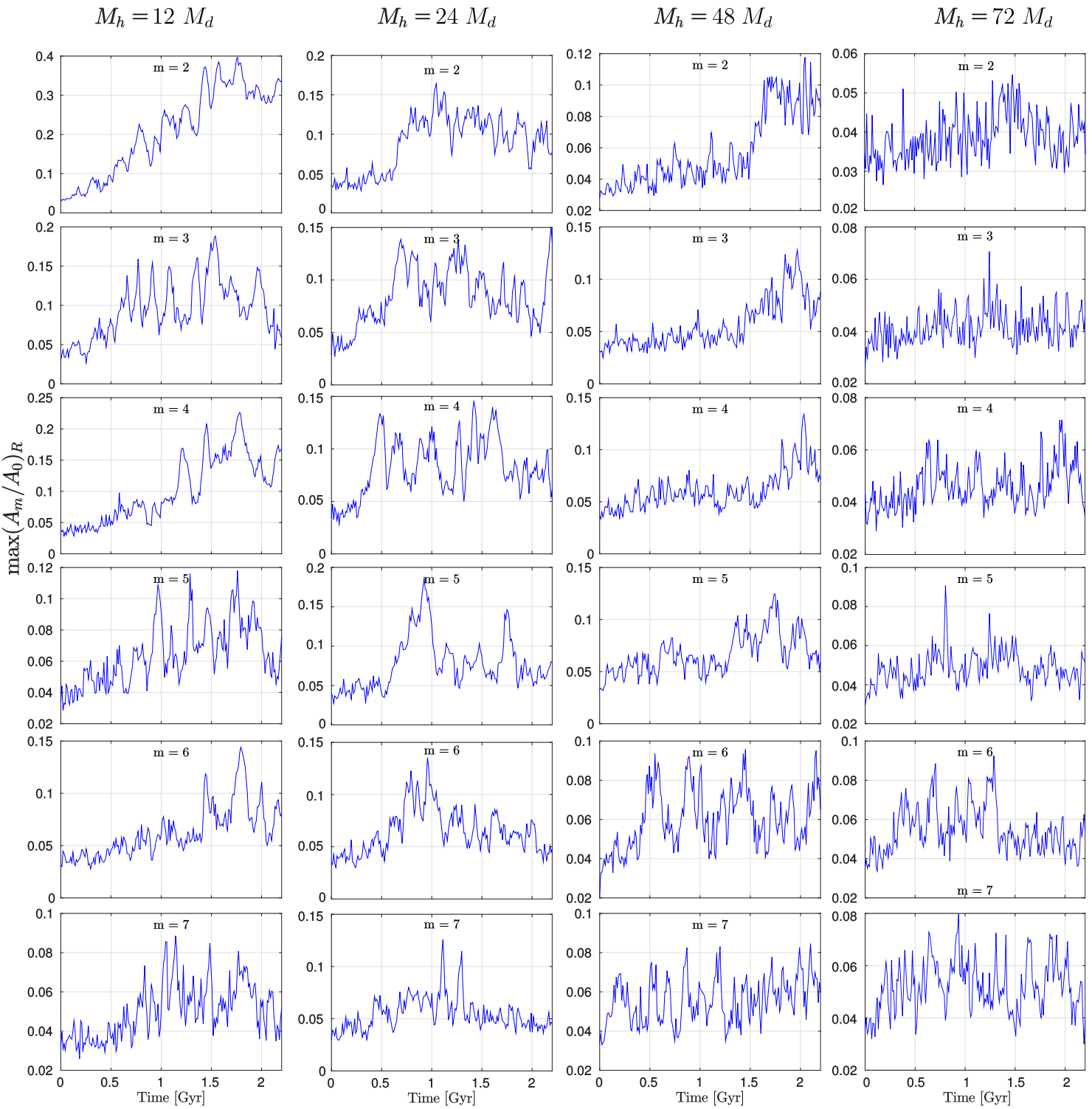

Figure 4.4: Amplitude ratios of identified Fourier modes for the same four simulations as specified in figure 4.3 in the same order as well. The modes are the same and the axes now show amplitude ratio over time. The plot when compared to figure 4.3 confirms that spirals become weaker with a heavier halo mass and larger mode.

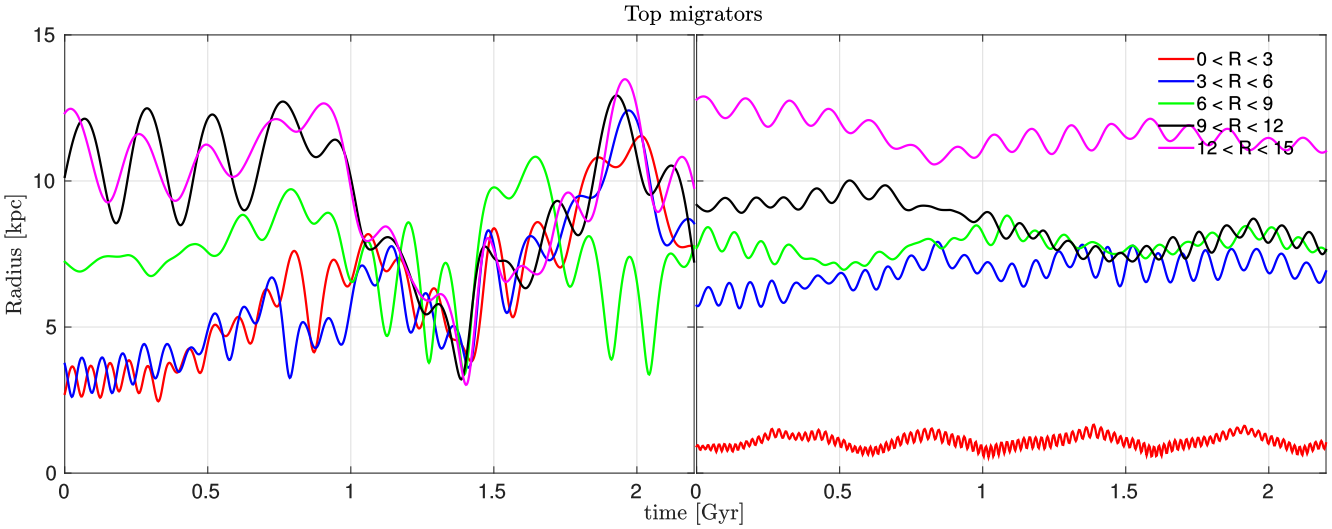

Figure 4.5: The top migrators in various radius bins for the 12 $M_{\rm d}$ halo and 72 $M_{\rm d}$ halo simulations. The former is on the left and the latter on the right. The strength of the individual migrations with a lighter halo causes migrations across almost the entire disc. For the heavier halo the migrations are much smaller.

Different spirals arise in the various simulations that are performed and a summary of the most prominent spirals are seen in table 4.1. We can see the decreasing strength of spiral arms as the halo mass increases, which was mentioned above.

Beyond appearance the difference in halo mass, and the different spirals that arise, has a noticeable effect on radial migration. Different levels of migration appear and can mix the galaxies significantly. When I extract the, cumulatively, largest migrators, for bins in 3 kpc radius, figure 4.5 is made.

The figure shows that when we have very stable systems or a massive halo we can still see radial migration up to about 2 kpc. In the lighter halos we see migrations that span across almost 10 kpc. This is evidence that in my simulations the width of available distance for migration is large. But this is for the farthest migrators which is only a few of the particles available. Figure 4.6 offers a better overview of the migration that occurs.

Table 4.1: Dominant modes and strengths of spirals in different simulations. The values summarise results from figures 4.3 and 4.4 that lower halo masses give stronger spirals and lower modes.

Simulation	Dominant m	A_m/A_0
12 $M_{\rm d}$	2	0.40
24 $M_{\rm d}$	5	0.20
36 $M_{\rm d}$	4	0.10
48 $M_{\rm d}$	4	0.15
72 $M_{\rm d}$	6	0.10
$N_{\rm bodies} = 2 \cdot 10^6$	5	0.20
$N_{\rm bodies} = 10^7$	3	0.15
$Q = 1.2$	4	0.25
$R_\sigma = 2$	5	0.1
Seed 1	2	0.15
Seed 2	4	0.15

In figure 4.6 we can see the behaviour of the entire disc. The same lightest and heaviest dark matter halo simulations are shown on the top and bottom panels respectively. Some noticeable differences are the range of available L_z values, the spread in ΔL_z, the shape of the figures and the regions with larger densities. As a heavier halo is used, a larger L_z value corresponds to the same radius as a smaller one would have in the lighter halo simulation. We can also see that the heavier halo mass simulation has no counter-rotating stars which is due to its stability. Roughly speaking the zero and maximum values of L_z in each case are at 0 and 15 kpc respectively. That the spread in ΔL_z is different is simply because migrations are much less common and less effective when we have weaker spirals in the heavy simulation. This can also be seen in figure 4.5.

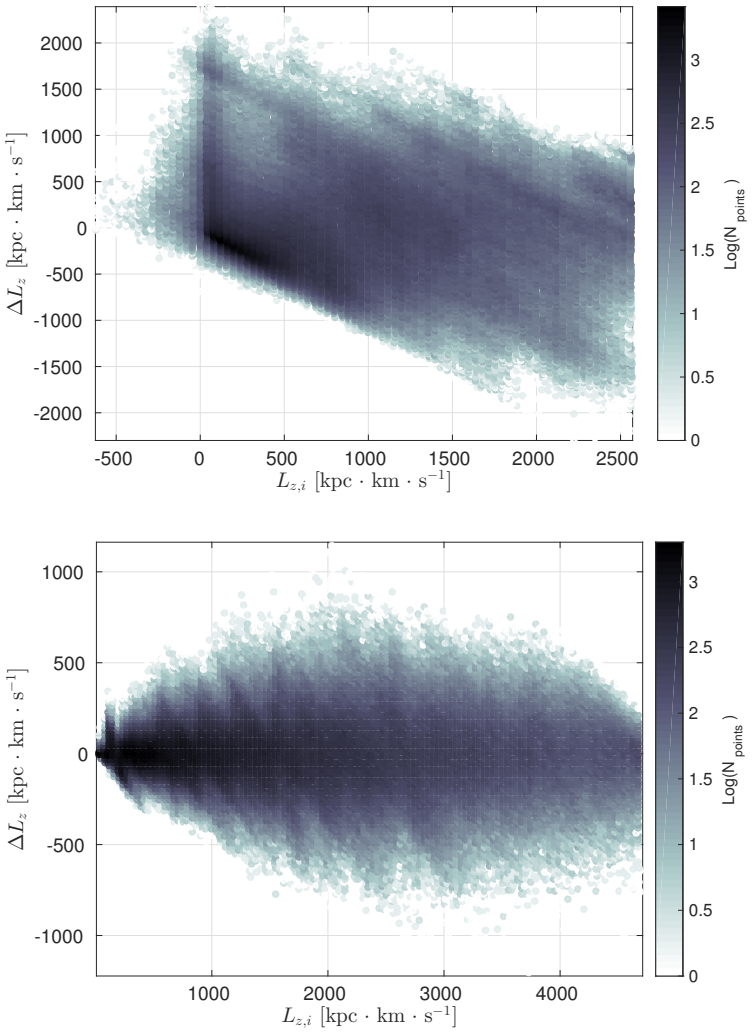

Figure 4.6: Showing $L_{z,i}$, the initial angular momentum in the z-direction, against the change in the same parameter from the start to the end of the simulation. Once more a 2D bin with 90x200 cells where the colour correspond to the logarithmic number of particles. *Top:* 12 $M_{\rm d}$ halo simulation showing large migrations throughout the disc. *Bottom:* 72 $M_{\rm d}$ halo simulation with much less impressive migrations and with the largest migration occurring near the middle of the disc.

The diagonal line appearing in the upper plot which seems to follow $\Delta L_z \propto -L_z$ is due to stars or particles with a given L_z rarely decrease to below zero angular momentum. If they do, they become counter-rotating stars which is why some stars lie below the diagonal line as well.

A key feature of these plots is that they reveal spiral features that otherwise might be difficult to find by eye in plots like figures 4.1 and 4.2. There are a number of diagonal lines, overdensities, appearing in both discs. These are the spiral arms and they appear as diagonal lines because of the migration that occurs interior and exterior to the corotation radius. A spiral has corotation radius at a certain L_z and at this point stars will not migrate, i.e. $\Delta L_z = 0$. Stars at lower L_z are interior to the spiral arm and will be migrated outwards, with a positive ΔL_z. Stars at higher L_z are exterior and migrate inwards with negative ΔL_z. This is just as churning is described in

section 2.4.

These figures show a difference in the number of spiral arms that arise in each of the two simulations as there are far more diagonal lines in the bottom plot of figure 4.6. This is also tied to the amount of radial migration as the upper plot has a span in ΔL_z of $\sim$4000 kpc km s^{-1} and the lower plot only $\sim$1500 kpc km s^{-1}. This confirms earlier findings about the correlation of modes, spiral arm strength, and migration.

From these plots it is evident that in our simulations the level of radial migration is tightly linked with the formation of spiral arms. Fewer and stronger arms cause more radial migration and stars move across vast distances in the simulated galaxies. It is also apparent that the mass of the dark matter halo has a significant effect on what spirals form and therefore also on the quantity and nature of radial migration that occurs.

4.2 Radial migration as a function of height z

As mentioned in section 3.2.4 there exists a discrepancy in the results of Solway et al. (2012) and Vera-Ciro et al. (2014). The results regard the effect that typical height above the disc, z, will have on radial migration. Solway et al. (2012) found minor differences between the angular momentum changes of stars belonging to the thick and thin disc. Vera-Ciro et al. (2014) found that migrators in their simulation are a heavily biased subset of stars that have lower vertical velocity dispersions (However I note from my results that different combinations of parameters such as surface density and Toomre's Q can change the velocity dispersion). A suggested explanation for this is that when a star is further away from the disc, it will not interact as strongly with the spiral arm. However these two simulations vary significantly in the halo mass. They have:

$$\left(\frac{M_{\text{halo}}}{M_{\text{disc}}}\right)_{\text{Solway}} \approx 0.9 \qquad , \qquad \left(\frac{M_{\text{halo}}}{M_{\text{disc}}}\right)_{\text{Vera-Ciro}} \approx 52. \tag{4.1}$$

With the latter using a Hernquist model and the former a rigid halo without well-defined profile, which we will elaborate on below.

The halo of Solway et al. (2012) is best understood through figure 4.7. The figure shows figure 1 from Solway et al. (2012) but with the dark matter contribution highlighted. It shows initial surface density profiles of their thin and thick tapered discs as black and green respectively. The dashed red curves are expected surface densities from the integration of their distribution function. The dotted curves correspond to non-tapered discs. The blue line indicates an adopted exponential profile of the thin disc. The point of this figure is that Solway et al. (2012), in order to achieve the dotted lines, must add dark matter to their halo. But we can see that for most of the disc radius, the contribution is exceedingly small so that in the disc the matter not part of the dark matter halo strongly dominates. This way of adding dark matter also means that the halo they use is not of a standard profile.

In Vera-Ciro et al. (2014), figure 1, a plot is provided which shows the circular velocity, v_{c}, as a function of radius for the disc, the halo, and in total. By taking a ratio of the circular velocity contribution of the disc and halo at 8 kpc, I can perform a comparison with my own simulations as well as find out what type of matter dominates since $F_{\text{c}} = mv_{\text{c}}^2/r \Rightarrow F_{\text{h}}/F_{\text{d}} = (v_{\text{c}}^{\text{h}}/v_{\text{c}}^{\text{d}})^2$ (here h and

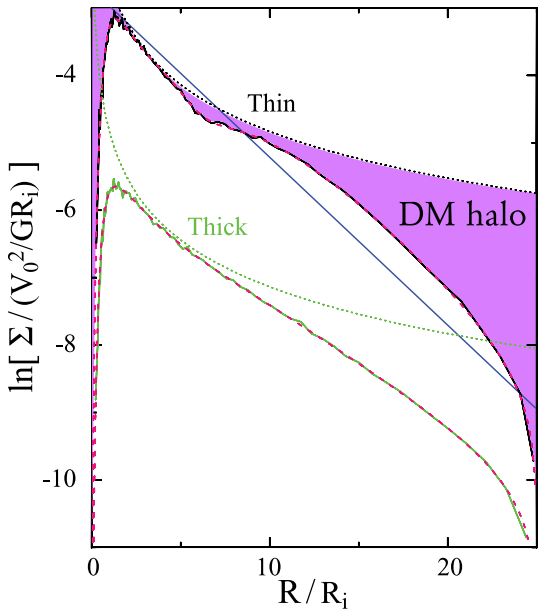

Figure 4.7: Figure 1 of Solway et al. (2012) showing initial surface density profiles of tapered thin and thick discs as solid lines, untapered discs as dotted lines, an expected surface density as red dashed curves, and a blue line which indicates an adopted exponential profile of the thin disc. The figure is highlighted here to show the contribution of the dark matter halo.

d stand for halo and disc respectively). The result is that the ratio from Vera-Ciro et al. (2014) is

$$\left(\frac{F_\mathrm{h}}{F_\mathrm{d}}\right)_{R_\odot} \approx 2.5 \tag{4.2}$$

by an eye measurement. Even with some uncertainty in the precision of the number it shows a very heavy DM halo that dominates the disc. This is in strong contrast to Solway et al. (2012).

The proposed explanation for the discrepancy in relevance of vertical motion is that the weaker the force from the halo the stronger the force from the spiral arm on a point in the simulations. A stronger spiral arm is likely to cause radial migration at larger distances from the midplane. Not only this, but a stronger disc tends to form fewer spiral arms. With more spiral arms close to each other in radius, the interactions of two could cancel out. In order to test the hypothesis that these two results differ because of their rather different halo masses we perform a number of simulations where we try halos of various masses. They have 12 M_d, 24 M_d, 36 M_d, 48 M_d, 60 M_d, and 72 M_d where M_d is the mass of the disc. We assume a Milky Way mass of $M_\mathrm{d} = 5 \cdot 10^{10} M_\odot$. The simulations have a constant $Q = 1.5$. All of these simulations have already been shown in section 3.1.3 and their force ratios between the halo and disc can be seen in table 4.2.

Table 4.2: The various halo mass simulations and their force ratios.

Simulation	$(F_\mathrm{h}/F_\mathrm{d})_{R_\odot}$
12 M_d	0.49
24 M_d	0.99
36 M_d	1.49
48 M_d	2.01
60 M_d	2.53
72 M_d	3.08

The result of performing the analysis in section 3.2.5 can be seen in figures 4.8 through 4.13.

As predicted, for the low halo mass galaxies there is no significant difference in migration for stars of different vertical velocities and then as the halo becomes more massive a stronger slope appears. To better verify the strength of the slope I perform a weighted least squares fit to fit a line through the points. The slopes are then plotted in figure 4.13. In order to get weights, I make the assumption that the population is Gaussian in order to calculate the dispersion of the standard deviation as

$$D[s] \simeq \frac{s}{\sqrt{2(n-1)}}, \tag{4.3}$$

where s is the sample standard deviation ($\sigma_{\Delta L_z}$ in my case) and n is the number of points in each standard deviation. The weights are then taken as the inverse square of D,

$$W_i = \frac{1}{D_i^2}. \tag{4.4}$$

As figure 4.13 shows, as the halo becomes more massive the magnitude of the slope increases in almost all parts of the disc. The innermost part of the disc is less clear. The actual value on the y-axis is not relevant here but rather the fractional increase between the slopes. This is because the value only speaks to the level of radial migration rather than the type. It was already shown in section 4.1 that a lighter halo has stronger migration. Here it is instead relevant what parts of the galaxy are undergoing radial migration, not how strong it is.

The velocity v_z changes during radial migration as a particle can move to a less or more dense region. Not only this, but it is also an oscillating variable and because of this adds some extra uncertainty to the slopes. To try and view the same behaviour in another fashion the vertical properties are also investigated in terms of vertical position z. This is shown in figure 4.14. Reassuringly it shows the same behaviour and for all parts of the disc.

The vertical height, z is not ideal either. It too is oscillating and as a star migrates it might no longer reach the same z in the new region it has entered. For this reason it is instead better to use a combination of the two, J_z, the vertical action which is an expression of the vertical oscillation. Actions are described in greater detail in section 2.4. To calculate actions from the output parameters of the code a pre-existing script has been made which is based on the work of Binney (2012). The action does not oscillate like the two other parameters and is therefore a more optimal variable for this investigation. It also serves to combine the results of the two previous figures. The result of using J_z is shown in figure 4.15. The description of results in J_z also makes for results more easily utilized by analytical models which have an easier time using actions than N-body simulations. An example of this is Schönrich & McMillan (2017).

The result from figure 4.15 is that a decreasing slopes is observed with increasing halo mass for all parts of the galaxies except perhaps the very outer parts. In all three different parameters used, z, v_z, and J_z, we are able to observe the appearance of a strong negative slope with heavier halo mass. This means that a heavy halo (or weak disc), does not migrate particles high above the disc as much as those near it. For the lighter halo and stronger disc, all vertical parts of the disc are partaking in migration to almost equal amounts. This corresponds to the two different cases described in the papers by Solway et al. (2012) and Vera-Ciro et al. (2014) as they had a light and heavy DM halo respectively. These results show a clear explanation for the discrepancy between the two papers as well as describe the behaviour of radial migration as a function of DM halo mass.

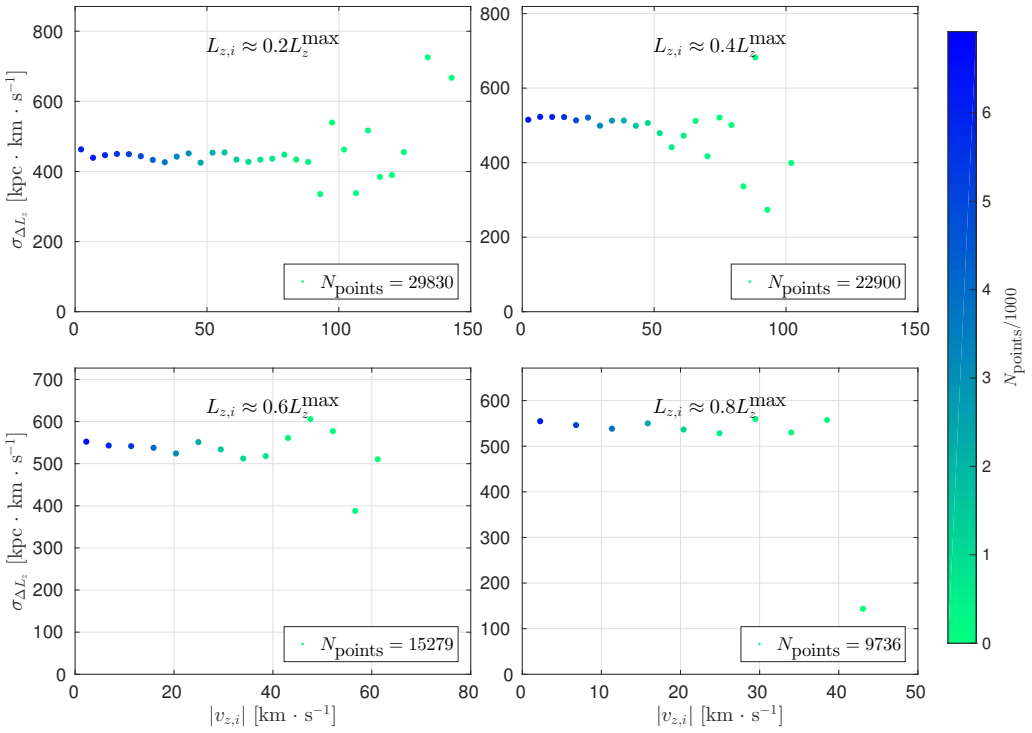

Figure 4.8: The plots resulting from the analysis tool described in section 3.2.5. It shows the absolute value of initial z-velocities against the dispersion in the change in angular momentum for four different regions of the disc. The colour shows how many points are in each of the calculated dispersions. This figure shows the 12 M_{d} simulation and an almost flat relationship. In the following plots up until figure 4.13 the slope will increase.

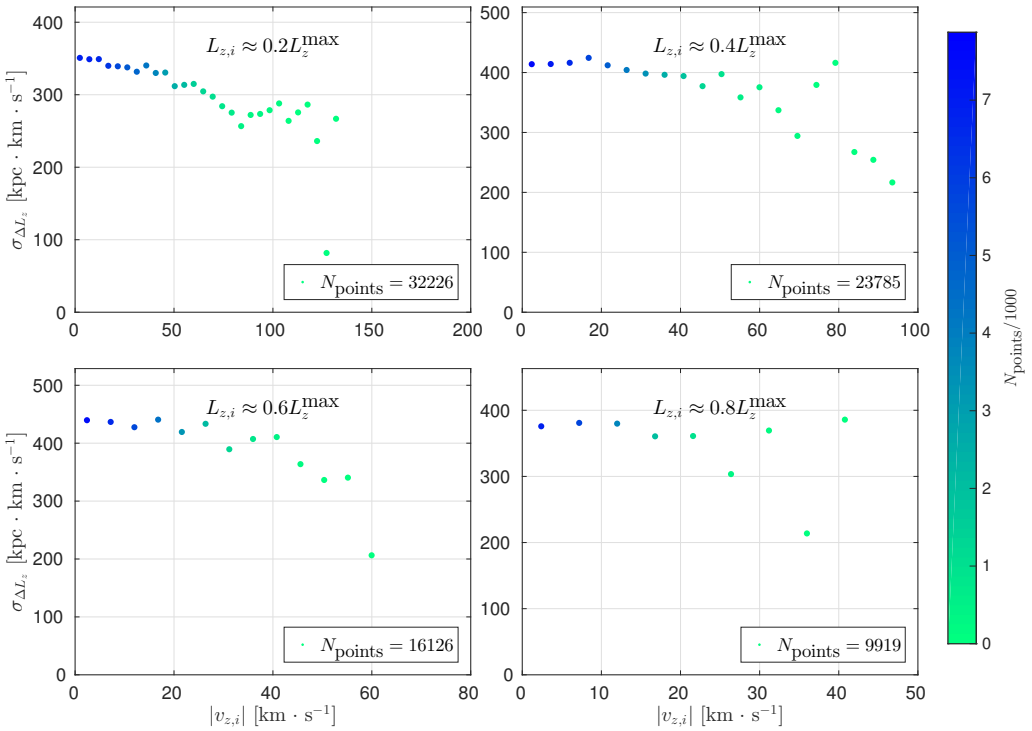

Figure 4.9: Same as figure 4.8 for the 24 M_{d} simulation.

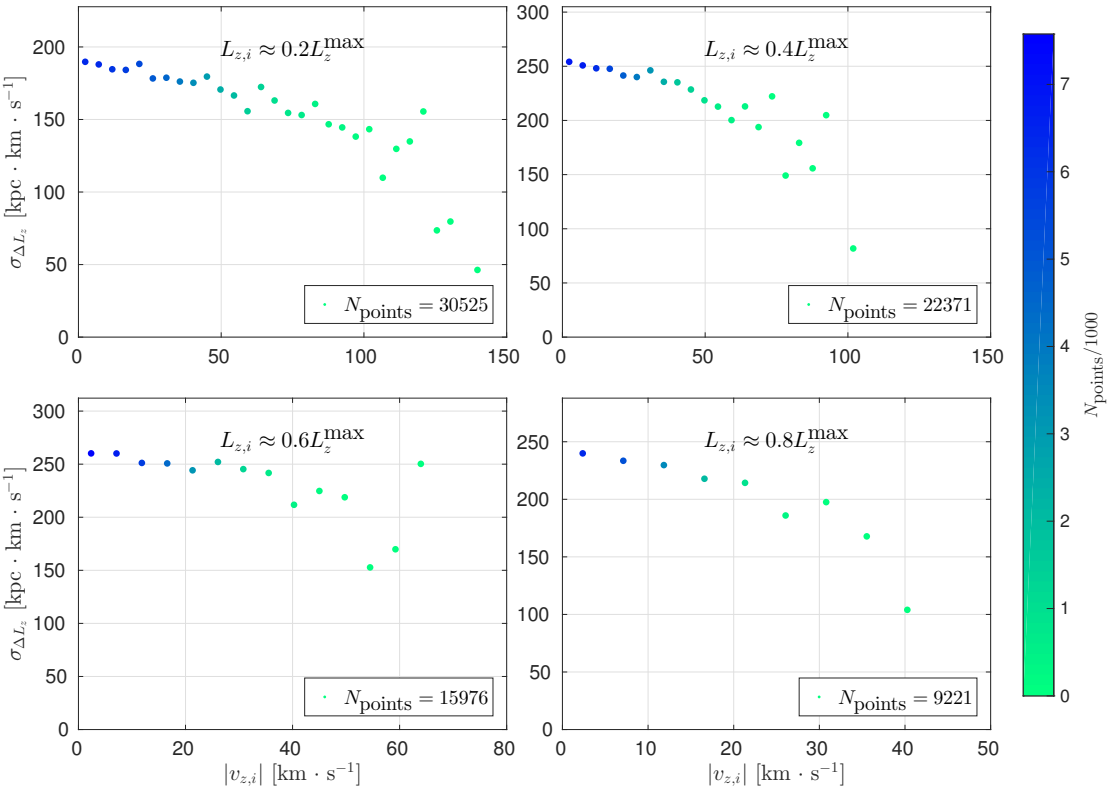

Figure 4.10: Same as figure 4.8 for the 36 M_{d} simulation.

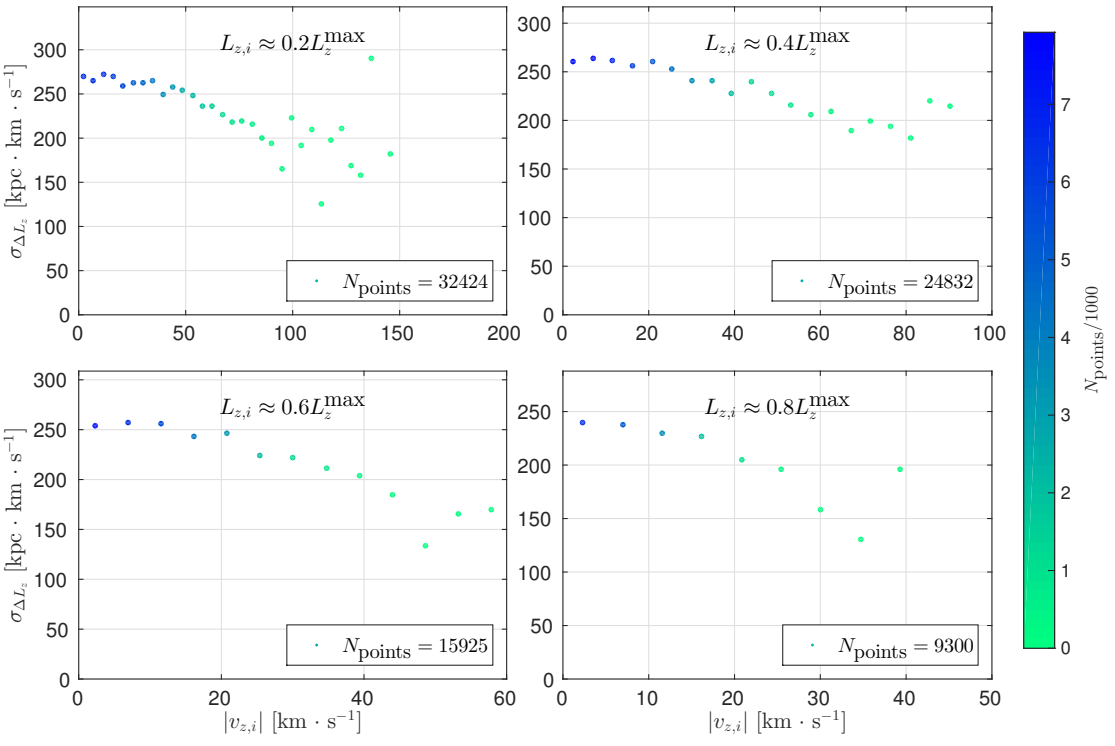

Figure 4.11: Same as figure 4.8 for the 48 M_{d} simulation.

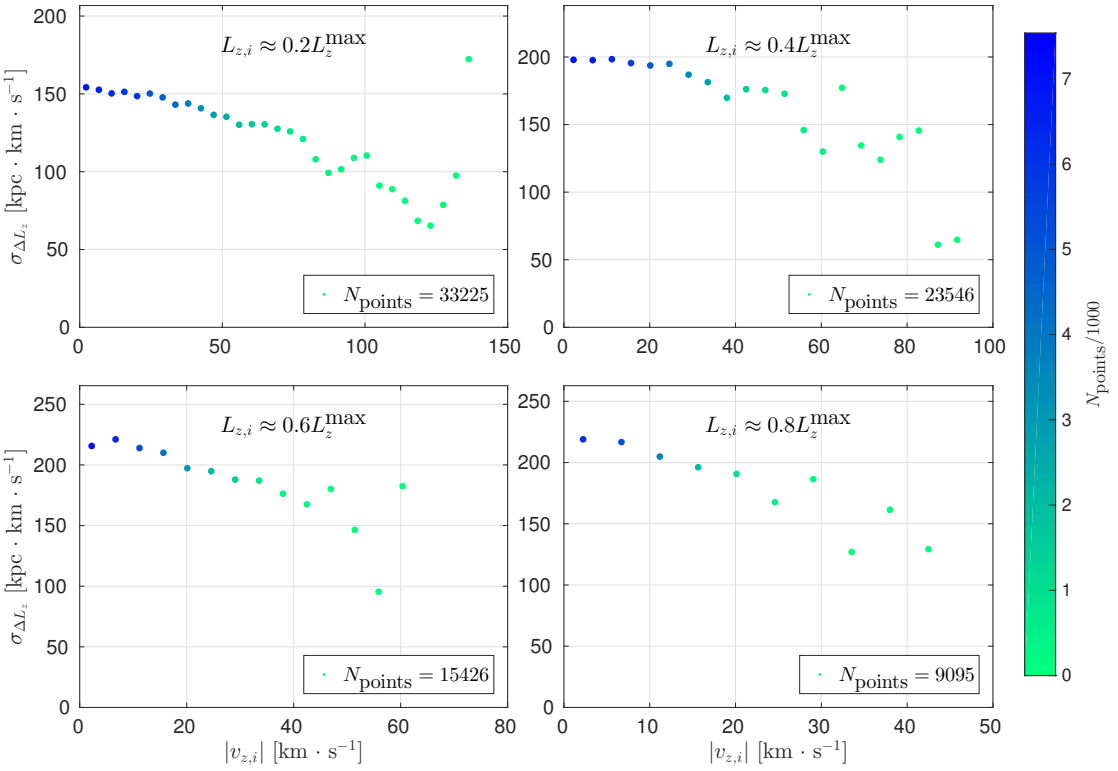

Figure 4.12: Same as figure 4.8 for the 60 M_{d} simulation.

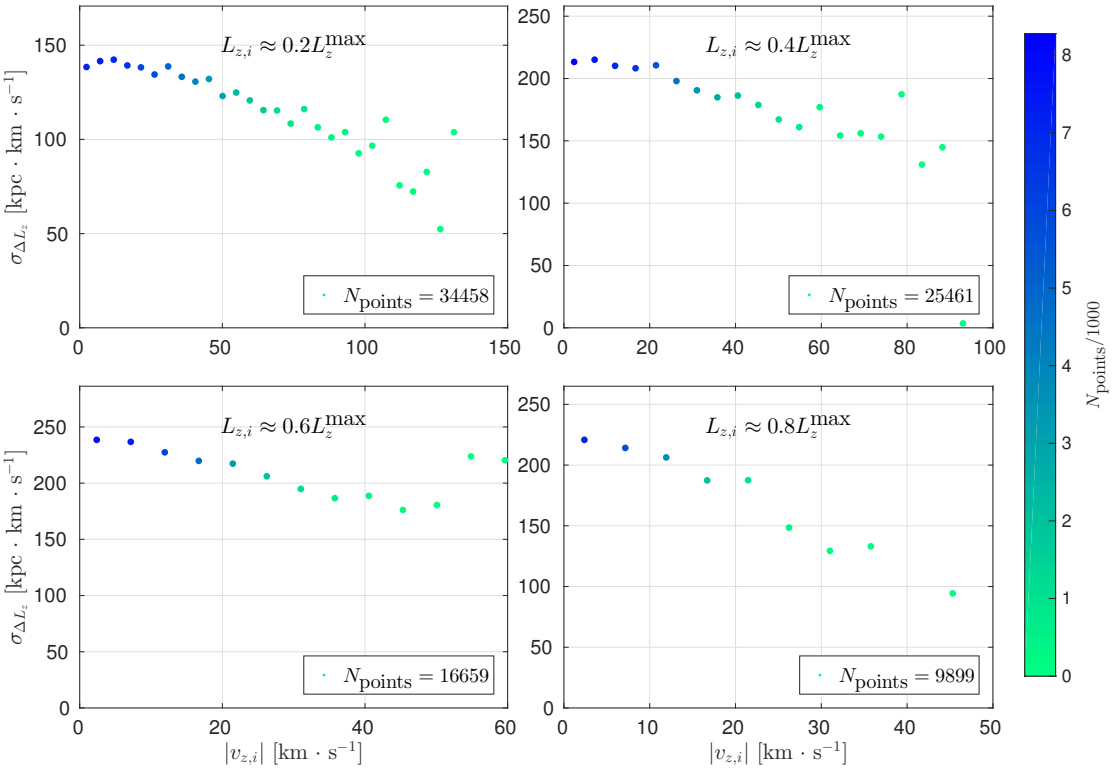

Figure 4.13: Same as figure 4.8 for the 72 M_{d} simulation.

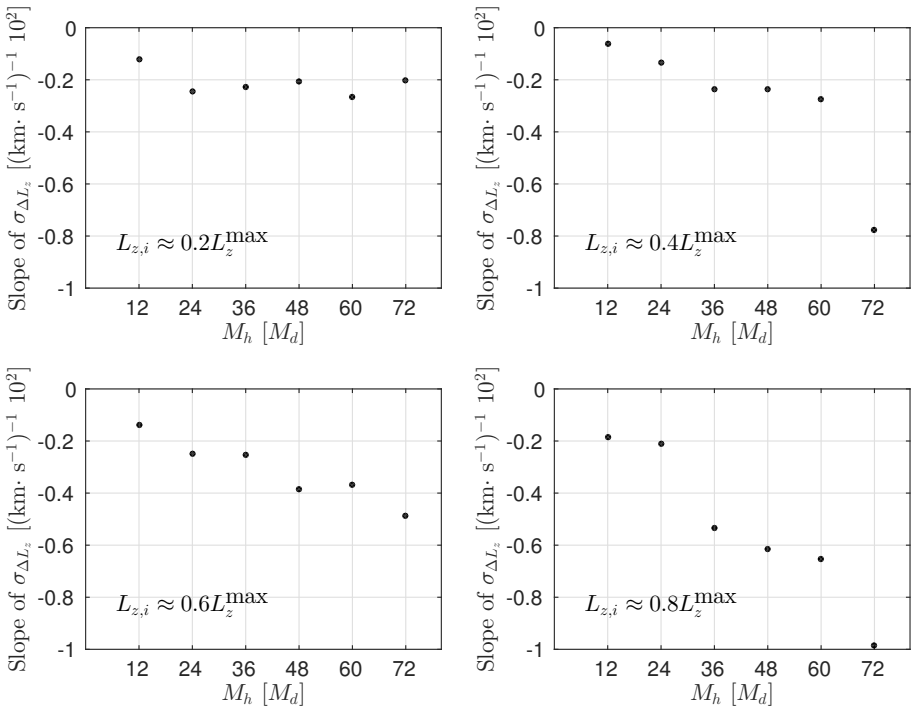

Figure 4.13: Derivatives of change in L_z with v_z, normalised such that the $\sigma_{\Delta L_z}$ value at $v_z = 0$ is 1 in all cases. There is a clear relationship between the slope and increasing halo mass.

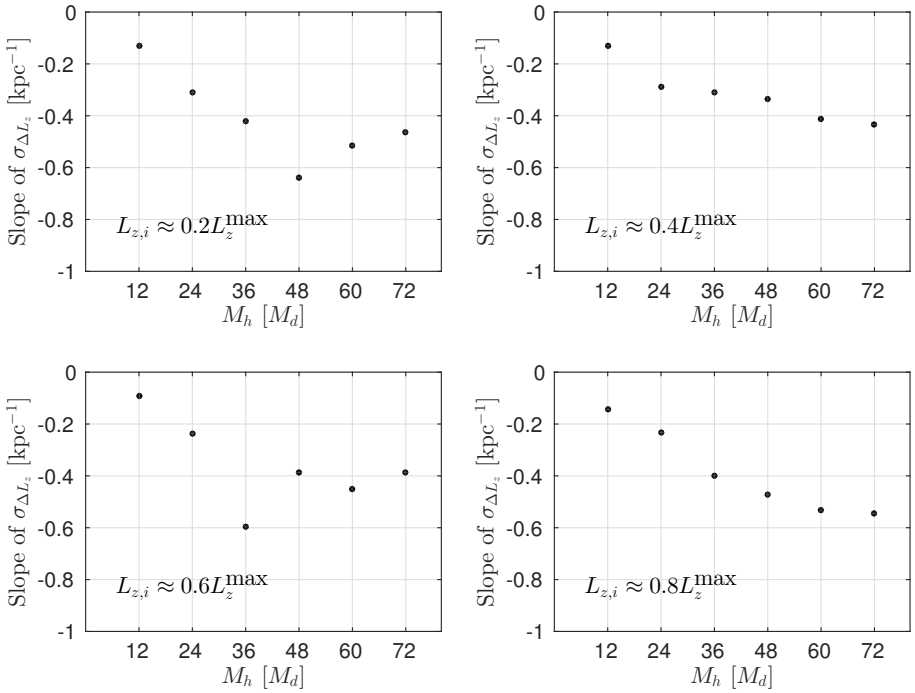

Figure 4.14: Similar to 4.13 but using the behaviour of ΔL_z with respect to position z rather than velocity v_z. The same pattern of an increased slope with halo mass appears here as well.

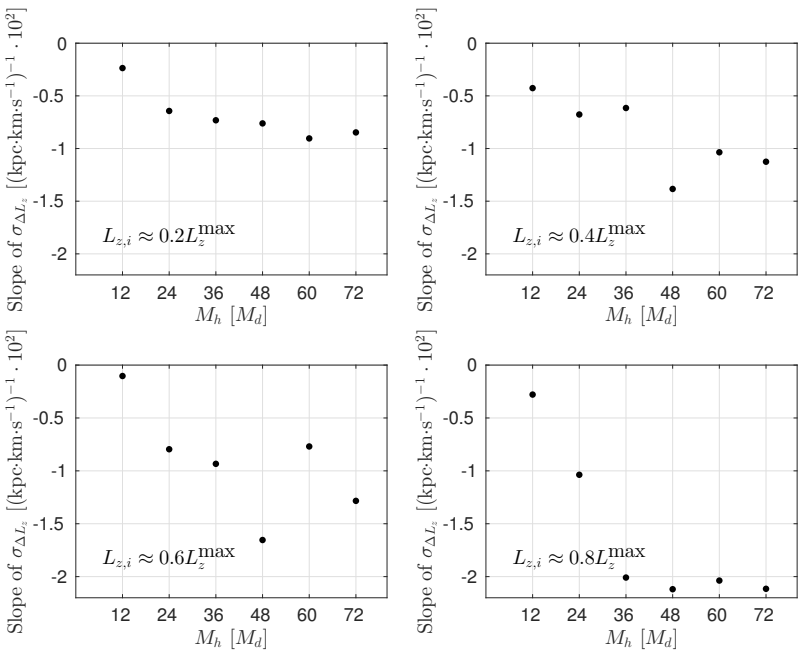

Figure 4.15: Also similar to 4.15 with the combined properties of vertical position and velocity, the vertical action J_z, instead of one or the other used to find the slope. As both figures 4.13 and 4.14 showed a relationship between slope and halo mass, it is not surprising to find the same pattern here.

4.3 Metallicity distribution function

Using the method in section 3.2.8 I am able to generate metallicity distributions for the SN in the hopes of being able to provide a path for predictions to be made in more expansive future work. However these results are attained with a very crude method and should not be considered predictions but rather they are indications of how a connection to observations can be made from pure N-body simulations such as these.

All the stars that end up in a region between 7.5 and 8.5 kpc are selected and treated as the 'solar neighbourhood' of the simulated galaxies. Painted with equation (3.21) and split into three different vertical regions, three different histograms are created from the 12 $M_{\rm d}$ mass halo and the 72 $M_{\rm d}$ mass halo to show the extremes of the two cases of churning that are observed (the disc-restricted or not, see section the 4.2). The result can be seen in figure 4.16. For a comparison the initial metallicity distribution is also shown in figure 4.17.

Some features will strike the reader immediately such as the positions of the peaks in each plot and the widths of the distributions. Starting with the upper plot of figure 4.16 with the lighter halo we can see that the peaks are shifted to higher metallicities and that the distributions are broader than they were in the initial distribution of figure 4.17. This is due to the effects described in section 4.2 that migration can occur at very different heights above the disc. Thus all parts of the disc end up being mixed and broadened. The more broadened they are the more the peak will move towards a galactic mean in metallicity. We observe different effects for the heavier halo where the distributions closest to the disc and furthest away share almost no stars of the same

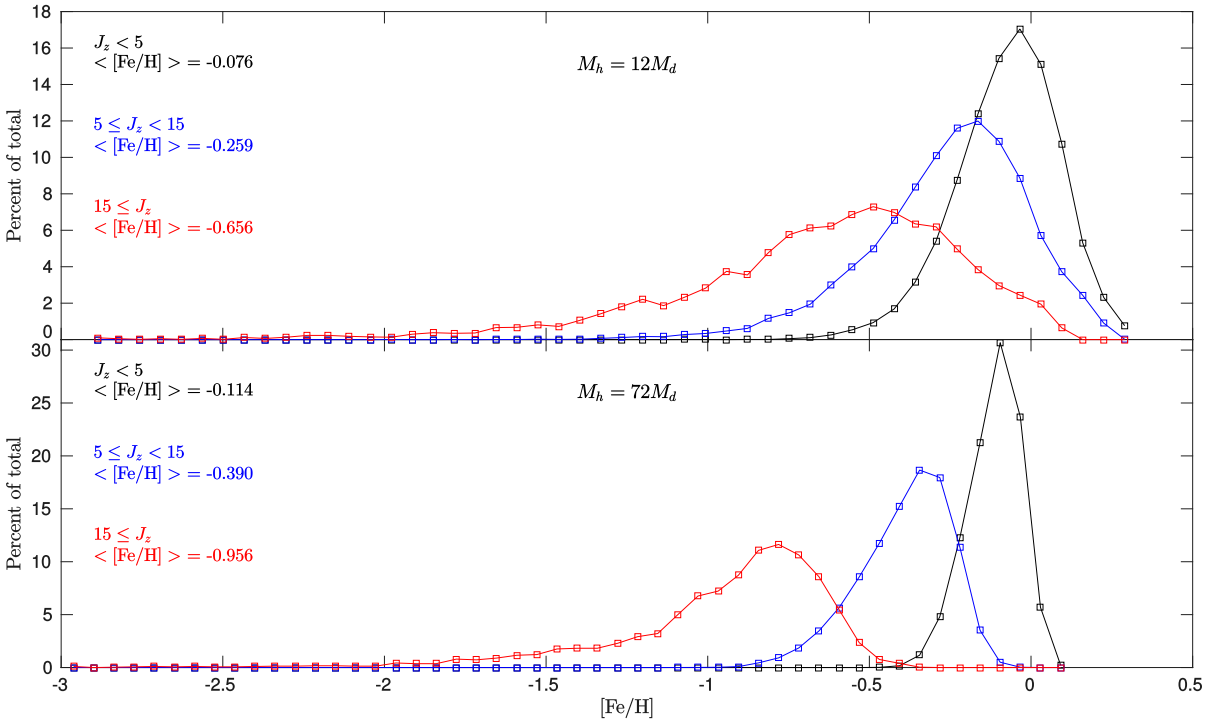

Figure 4.16: Metallicity distributions of the SN for the lightest and heaviest halo mass simulations at the end. The halo mass, J_z bin, and mean value of the distributions are indicated in the figure. For the lighter halo, with more migration, a broader width is seen for all vertical slices of the disc. For the heavier halo the broadening is much less, as would be expected with less migration.

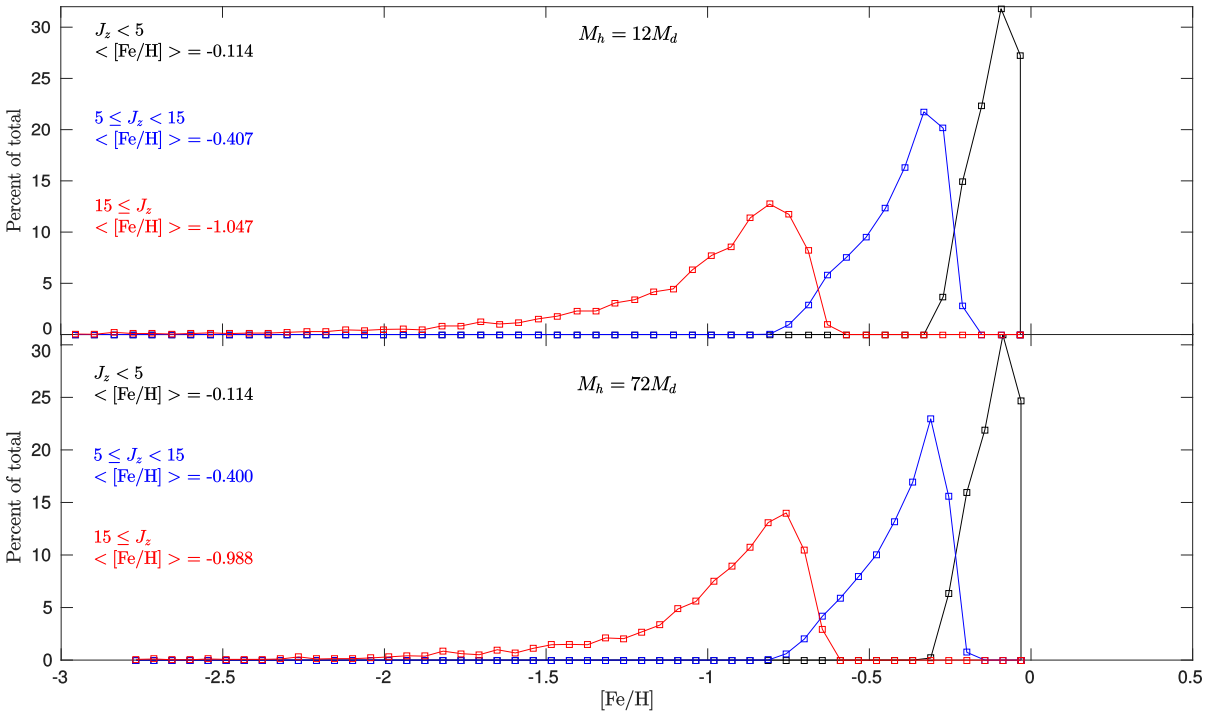

Figure 4.17: Same metallicity distributions as 4.16 but taken at $t = 0$ for the SN. There is almost no difference as no mixing has occurred.

metallicities and the distributions are not shifted towards the right. They also appear far less mixed as they retain almost the same distribution as they initially had.

The relative widths of distributions in the same simulation should be carefully explained so as to not be misunderstood. In the heavier halo mass simulation we expect very little migration to be occurring for the stars located at larger vertical action, yet the relative width is larger than for the stars close to the disc. This is likely due to the fact that a larger span of J_z values are considered. The lowest vertical segment is only 5 kpc km s^{-1} wide, the next one 10 kpc km s^{-1} and the final one contains all values above 15 kpc km s^{-1}. This would likely broaden the distributions and therefore the width does not imply that the upper parts perform more migration.

When drawing input from Hayden et al. (2015), averages of their measured values are used. The result presented here can, however, also be compared to Hayden et al. (2015), by considering the complete width of their data to observe the level of mixing. The extent of the distributions being between 0.5 and 1 dex is comparable to the extent of MDFs presented in Hayden et al. (2015), which shows that the level of mixing might be within the realm of possibilities. This exercise into including metallicities shows a small example of how the path to observational comparison might be possible for results from pure N-body simulations like mine. However I again stress the very simple nature of these metallicity properties.

4.4 Simulation sensitivity

Due to the inherently chaotic nature of N-body simulations it is important to ensure that the results hold if subjected to further testing. Stochastic variations can occur in large simulations (Sellwood & Debattista 2009) and in order to test the simulations found in this thesis I use different numbers of particles, run simulations for various lengths, and utilise several different seeds. I also undergo test of the dynamical stability of the simulations. The results of this will now be presented.

4.4.1 Changing Toomre's Q

In section 3.1.3 the role of Toomre's Q parameter was discussed. One investigation that has been performed is changing its value, but still keeping it constant for the initial conditions, or by setting $R_\sigma \neq 0$, allowing it to vary with radius. Three simulations are performed. The first two are set $Q = 1.2$ or $Q = 3$ throughout the disc, while the final one has $R_\sigma = 2$ and a variable Q. All use a halo mass of 24 M_d. Focus is put on the stability of the simulations under the different initial conditions as well as migration and they are only analysed up to 1.1 Gyr of evolution.

Figure 4.18 shows the moving standard deviation from section 3.2.2 for the three simulations. Note that in the centre the proportionality in equation (3.10) no longer holds. With higher Q comes a larger velocity dispersion as can be understood through equation (3.9). Figure 4.18 confirms this as the σ_R values differ. Previous statements regarding the stability provided by a larger value of Q are also shown to hold true as the $Q = 3$ simulation clearly experiences very little dynamical heating in the radial direction after even 1.1 Gyr. The same cannot be said for $Q = 1.2$, which experiences some heating, albeit to a small extent. The 24 M_d DM halo simulation of section 4.2 is comparable and shows similar heating which is not shown here. Having a fixed Q over all radii may not be representative of reality however as Q may change and when it

does the bottom plot is produced. The radial velocity dispersion is somewhere between the two other plots but remains as stable as the $Q = 3$ simulation. We do not expect to see any significant increase in non-circular velocities as a result of churning (Sellwood & Binney 2002).

We found in section 4.1 that a larger halo mass created a more stable system where parts of the disc could not easily interact with each other and form strong spiral arms. In the case of stability with Q the $Q = 3$ and R_σ the disc has larger radial oscillations and is dynamically hotter. This makes it more difficult to form spiral arms and can be similar in appearance to the heavy halo simulations. The $Q = 3$ simulation does not create any spirals that are identifiable, the $R_\sigma = 2$ forms a weak $m = 5$ mode, and $Q = 1.2$ creates a strong $m = 4$ mode. This can also be seen in table 4.1.

The levels of migration show the expected behaviour given the type of spiral arms that are seen. $Q = 3$ and R_σ experience very little radial migration. The former reaches roughly $\Delta L_z \pm 150$ kpc km s^{-1} and the latter reaches somewhat higher with roughly $\Delta L_z \pm 400$ kpc km s^{-1} which is still five times smaller than the light halo showed in section 4.1. The $Q = 1.2$ simulation shows roughly three times as much migration as the R_σ simulation with $\Delta L_z \pm 1500$ kpc km s^{-1}.

When it comes to vertical properties the slopes of $\sigma_{\Delta L_z}$ against $|v_z|$ are calculated for the four parts of the disc. For the $L_z = 0.2L_{z,\max}$, $L_z = 0.4L_{z,\max}$, $L_z = 0.6L_{z,\max}$, all three simulations show slopes of roughly -20, -30, and -40 for the respective regions. In the outer part with $L_z = 0.8L_{z,\max}$ the slopes are -15, -80 and -50 for the $Q = 1.2$, $Q = 3$, and $R_\sigma = 2$ simulations respectively, likely due to noise from having few particles in the outer parts. If compared to figure 4.13 these slopes are slightly more negative than the standard simulation. This may be due to the shorter duration for which the simulations are evaluated.

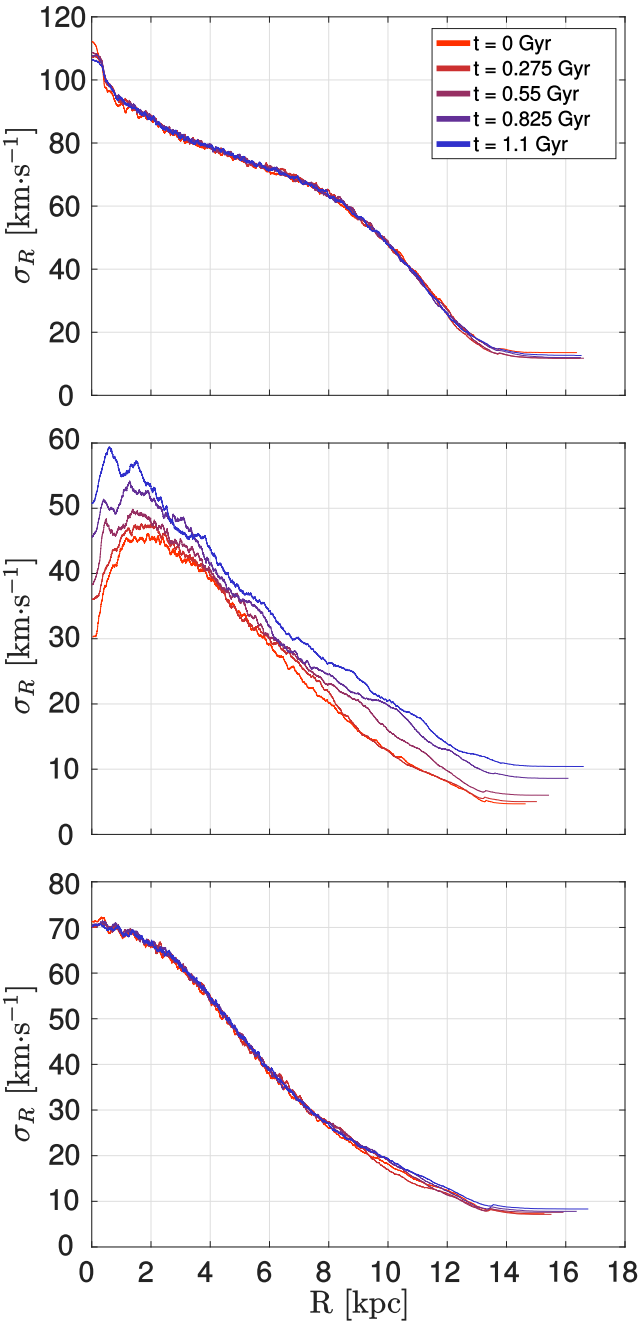

Figure 4.18: The radial velocity dispersion of three simulations using $Q = 3$, $Q = 1.2$, and R_σ in descending order. The standard deviation is calculated using a moving standard deviation as described in section 3.2.2. The colours of all three plots indicate different times during the simulation and a legend is shown in the top plot. The simulation with a high $Q = 3$ is clearly very stable as expected from the theory. The more realistic case of a variable Q through $R_\sigma \neq 0$ also behaves very stable.

4.4.2 Different N

The standard simulation consists of 10^6 particles and no results are drawn from simulations with fewer. Instead I attempt to see if more particles are necessary and have therefore performed simulations using $2 \cdot 10^6$ and 10^7 particles. These simulations use different seeds but apart from number of bodies identical input parameters as the 24 M_d DM halo, $Q = 1.5$ simulation.

The $N = 10^6$ simulation forms $m = 5$ spirals with amplitude 0.2. For the larger simulations with $N = 2 \cdot 10^6$ and $N = 10^7$ the values are $m = 5$ and $m = 3$ as well as 0.2 and 0.15 in amplitude respectively. The effect that this has on radial migration can be seen in figure 4.19 where the change in angular momentum is shown for the entire discs. All three simulations show significant radial migration with $\Delta L_z \pm 1500$ kpc km s^{-1} as is expected with a lower halo mass from section 4.1.

In figure 4.20 $|v_z|$ is plotted against L_z, both taken at the starting time of the simulation with the standard deviation of ΔL shown with colour. It gives a sense of how migration behaves over the entire disc as well reveal any vertical properties through v_z. Both plots reach equal extremes in $|v_z|$ for all L_z. It can be seen that migration takes place in most parts of the disc except the very inner parts. This is in agreement with results from Bird et al. (2012) although unfortunately they do not show the behaviour in their very inner disc which is where we find less migration. The amount of migration seems to stay the same as $|v_z|$ increases and drops off mostly at the edges of the coloured region. This aligns well with the vertical properties observed in the $N = 10^6$ simulation from section 4.2.

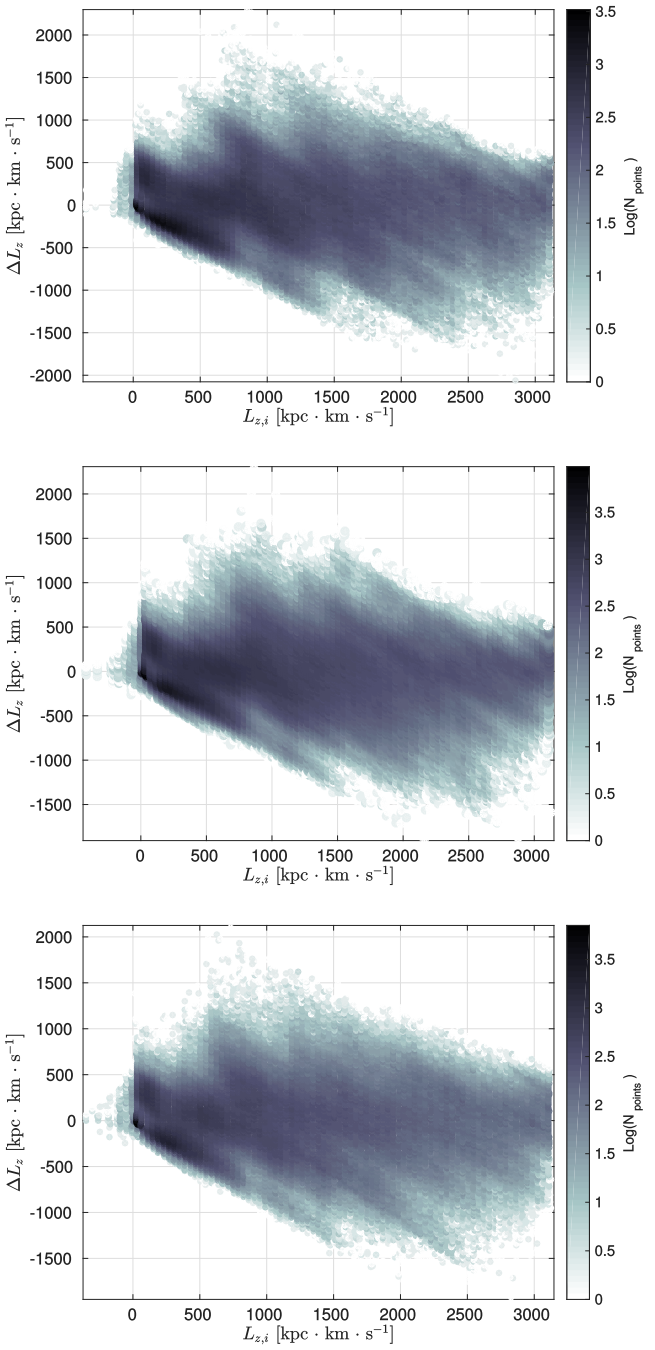

Figure 4.19: Number density of simulated galaxies with different number of bodies. Comparable to 4.6. *top:* Angular momentum changes of the $N = 10^7$ simulation. *Middle:* The simulation with $N = 2 \cdot 10^6$. *Bottom:* The standard simulation. The plots show the appearance of spiral arms as diagonal overdensities.

The three simulations with various bodies show similar extents of migration, reaching $\Delta L_z \pm 1500$ kpc km s^{-1} as well as similar strengths in spiral arms and some slight difference in the number of modes with two showing $m = 5$ and the other $m = 3$. The vertical properties are not affected by the increase either. This shows that our simulations are robust against changes in number of particles, allowing greater confidence in results drawn from 10^6 particles which reduces computational costs.

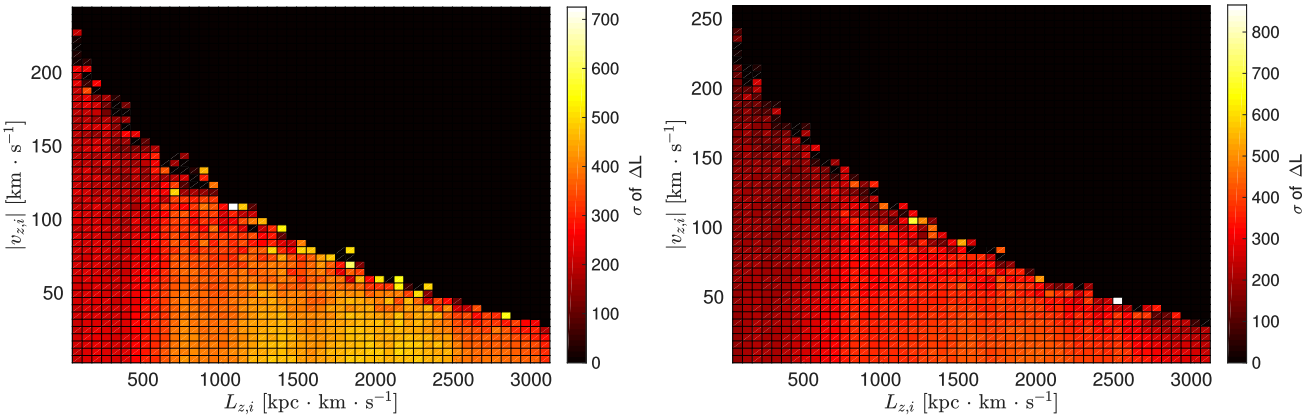

Figure 4.20: A 50x50 bin of $|v_z|$ and L_z at the start of the simulation with standard deviation of ΔL as colour map. *Left:* The $N = 10^7$ simulation with no noticeable effect with v_z except perhaps a weak decrease at the edges. *Right:* The $N = 2 \cdot 10^6$ simulation. It shows the same behaviour as the left plot.

4.4.3 Different durations

The simulations normally run to 2.2 Gyr. To learn whether or not this choice of duration for the simulation has an appreciable effect a simulation is run for 5.5 Gyr using a million particles and a 24 M_d DM halo. This simulation is then compared to one with the same initial conditions that runs for only 2.2 Gyr, the standard simulation. The natural first investigation is the behaviour of top migrators and can be seen in figure 4.21 for both simulations. The same behaviour is seen for the first 2.2 Gyr of evolution after which the longer simulation simply churns somewhat back and forth. The churning simply carries on in a similar fashion. We can see that no unpredicted new behaviour is revealed by the longer duration and the migrations are of roughly the same magnitudes, changing up to 6-8 kpc, and do so for all parts of the disc considered.

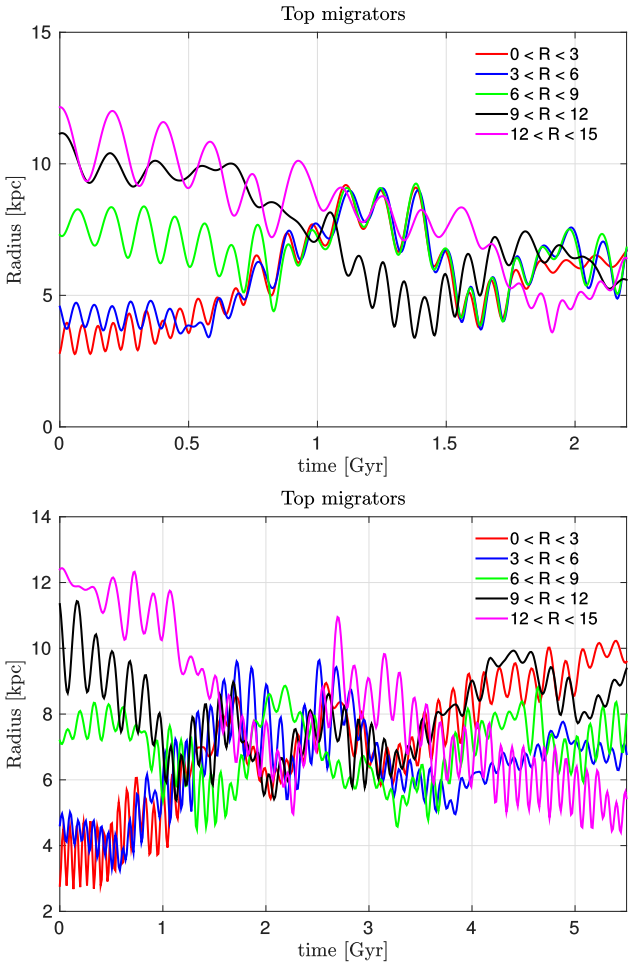

Figure 4.21: The top migrators for the standard simulation in the upper panel and the same in the bottom panel for the 5.5 Gyr simulation, both in different radial bins. No new behaviour is revealed at times later than 2.2 Gyr and instead stars move back and forth.

Other properties between the simulations are the extent of radial migrations seen in the ΔL_z and L_z space. Here they both reach $\Delta L_z \pm 1500$ kpc km s^{-1} and are difficult to distinguish. Both form $m = 5$ mode spirals with amplitude ratios of roughly 0.2. Regarding the vertical properties the

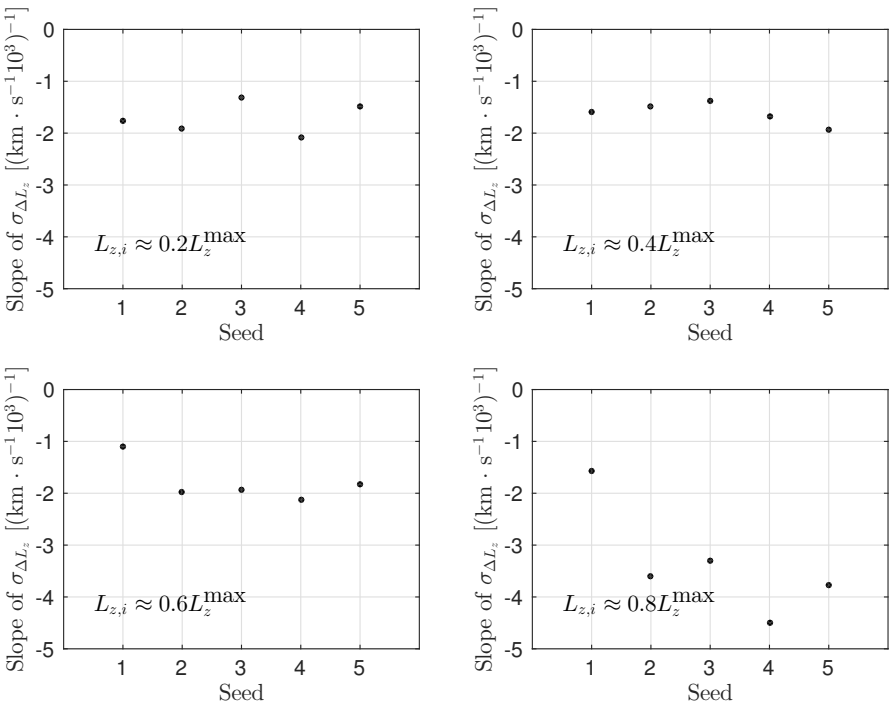

Figure 4.22: Slopes for different parts of simulated discs in $|v_z|$ against L_z, comparable to 4.13 and similar figures. However, the x-axis now contains the seed number instead. The numbering of the seeds is arbitrary. There is little scatter in the slopes apart from in the very outer parts, which means that the seeds are not too dissimilar.

slopes of $|v_z|$ and $\sigma_{\Delta L_z}$ are almost identical at -20 for all parts except the outer disc where the 5.5 Gyr simulation reaches -60. This could again simply be noise due to having less particles to determine the dispersion.

The multiple noted similarities between the simulations show that the simulations are not sensitive to much longer durations. Making simulations shorter runs the risk of missing information but longer than 2.2 Gyr does not change the outcome of the results. This, in addition to earlier results regarding the number of bodies, can significantly reduce computational cost and improves the robustness of the simulations.

4.4.4 Different seeds

When initialising a simulation a seed is selected based on the clock. However not all seeds need to generate good initial conditions. For this reason it can be useful to compare identical simulations started with different seeds. This would constitute a third addition to the robustness of the simulation along with number of modelled bodies and duration of simulations.

For a 24 M_d simulation 5 different seeds were tried. They each had 10^6 particles and were run for approximately 2.2 Gyr. In order to most conveniently show whether or not the seeds make a difference we investigate the slopes of $\sigma_{\Delta L_z}$ against $|v_z|$ once more but this time with identical halo masses and simply different seeds.

The result is in figure 4.22 and we can see that the slopes end up almost identical for all seeds with very little scatter. In the outer parts of the galaxies there is a larger scatter however. This is possibly due to there being less bodies in the calculation of the standard deviation as seen in similar earlier cases. Although a negative trend might be hinted, none exist as the order of the seeds is arbitrary and are placed in increasing numerical fashion for simplicity.

This result means that there is little variance between the seeds that are generated and it adds confidence to the results presented throughout this thesis as they are taken from a single seed. As such the robustness provided by this exercise is incredibly important for the entire presented results.

Chapter 5

Conclusions

In this thesis I present my work comprising of running numerous large N-body simulations with 1-10 million particles between 1.1-5.5 Gyr as well as a broad analysis of the output data. The simulations have been performed using the existing packages for N-body integration and initial conditions available through `NEMO` (Teuben 1995). To generate initial conditions the package `mkWD99disc` has been used which is based on Dehnen (1999). The integration is carried out by `gyrfalcON`, an integrator designed for specifically these types of simulations. The simulations are pure N-body apart from a dark matter halo external potential from Dehnen & McLaughlin (2005). The simulations have been performed with different various initial conditions with the prime goal being an investigation into radial migration as a function of vertical properties (z, v_z, J_z). To this goal I have simulated a range of different DM halo masses to produce spirals of different strengths and types. Other parameters investigated have been dynamical stability through Toomre's Q, simulation stability through various seeds, number of bodies, and different simulation lengths.

The analysis of the simulation data has been performed with MATLAB. Multiple scripts have been created to produce all the various plots available in this thesis, all of which are thoroughly described in section 3.2. The output produced gives time, mass, positions, velocities, and accelerations. All other variables need to be calculated from them. Tools have been developed to identify the top migrators at separate radii, calculate radial velocity dispersions, angular momentum and angular momentum changes, metallicity distributions, and Fourier spectra. Metallicity has been painted on to the simulation output taking inspiration from APOGEE results (Hayden et al. 2015) and are simply assigned to a certain particle. It is not evolved over the course of the integration. This means metallicity is not evolved and only mixed by the end of the simulations.

The importance of radial migration and the understanding of it is not to be underestimated. The results from the literature are quite clear that the observed spread in metallicity cannot be explained by a simple picture of isolated galactic evolution and a means of mixing in the Galaxy is required. There has been many solutions to provide the mixing required and we have given two examples: a break in star formation history (Chiappini et al. 1997) and large accretion events (Bensby et al. 2005). While these solutions are very possible, radial migration is going to be occurring as well if there are spiral arms present in the Galaxy (Sellwood & Binney 2002) and the Milky Way does indeed have spiral arms, although it is not clear exactly how many. Radial migration provides a mixing solution based in few approximations and which occurs without outside influence.

In this work a strong focus is put on identifying how radial migration works but also on where it occurs in the Galaxy in terms of vertical and radial properties. This type of analysis can carry on through other work which use analytical models that build on results like these to make assumptions about what migration to consider in a certain type of disc. Some examples of where analytical models of this type are used include Schönrich & Binney (2009) and Schönrich & McMillan (2017). Studies like these are the justification for approximations made in such analytical models.

This work helps to overcome shortcomings that exist within the literature on N-body simulations of radial migration. One of the shortcomings is that often only a single galaxy is simulated and studied (e.g. Vera-Ciro et al. 2014; Halle et al. 2015; Kawata et al. 2017). Studying a single galaxy puts strong limitations on the results produced and how they might be applicable. Another shortcoming to note is that when multiple simulations are performed for the same work, they are done so in a constrained environment (e.g. Sellwood & Binney 2002; Solway et al. 2012). This can be either by creating discs specifically to have certain behaviour or patterns such as a given m-mode spiral or a bar. This work seeks to take a step forward. While other studies such as those mentioned might be able to make more detailed claims or comparisons to observations this work aims to understand radial migration across very different simulations and types of simulated galaxies. To this end we have performed simulations that vary strongly from one another and even from what we believe the Milky Way ought to be like. This work exists partly to offer insight into what type of galaxy to simulate if one wishes to have a certain type of behaviour in their simulated system.

I have shown in section 4.1 a relationship between the stability of a system and the strength and number of spiral arms that appear. Things that stabilise the galaxy, such as an increase in Toomre's Q for the disc or a larger dark matter halo, create systems that are less sensitive to spiral density waves increasing and when they do, it is at a higher mode with a much lower amplitude. This also has a clear effect on the amount of migration. Figures 4.5 and 4.6 showed a remarkable decline in the amount of migration that occurs via churning with the existing spiral arms as changes of $\Delta L_z \pm 2000$ kpc km s^{-1} for the low mass halo decreased to $\Delta L_z \pm 500$ kpc km s^{-1} for the heavy halo mass case. Blurring too appears to decrease in amplitude somewhat as the radial oscillations go from around 4 kpc for the light halo to barely even 1 kpc in the heavy mass halo.

A major focus of this work is again on how the vertical motions of stars affect their radial migration. In section 4.2 I discuss the results of two papers from literature, namely Solway et al. (2012) and Vera-Ciro et al. (2014) where the former claims that stars in their simulations migrate mostly regardless of vertical properties and the latter claims an opposing conclusion that migrators have lower vertical velocity dispersions. I have been able to replicate similar results to each by using dark matter halos of varying mass, varying the stability and the spiral arms that form in each case. Vera-Ciro et al. (2014), which claim that vertical properties affect migration, have multiple spiral arms and high modes with a heavy dark matter halo. When I simulate a heavy dark matter halo, I also find lower strength but multiple arms and that vertical properties are far more important. Solway et al. (2012) have a $m = 2$ spiral in the simulation that leads to their claim. They also have a light halo. In table 4.1 we see that the lighter haloes create fewer and stronger spiral arms. This investigation into the varying DM halo mass offers an explanation to the discrepancy between these two papers and a solution of when vertical properties are of stronger significance.

I have investigated the effects of varying the radial velocity dispersion, parametrised through Toomre's Q on the simulated galaxies. The tested values were two fixed values of $Q = 3$ and

$Q = 1.2$ and one simulation where the value of Q varies with radius. The way in which Q varies with radius is described by equation (3.9) and the following paragraphs. It is not obvious that the Q parameter should be constant so we experiment with it to determine the simulations' sensitivity towards it. Figure 4.18 showed the effects of the various settings for Toomre's Q. The parameter is closely linked with dynamical stability we can see that the higher value gives a much more stable disc which changes little over the first billion years. The same goes for the case with a varying Q. When Q is set as low as 1.2 or 1.5, some increase of radial velocity dispersion is observed however it is not significant. This is in agreement with claims by Sellwood & Binney (2002) that churning does not cause significant increases in non-circular motion. Other processes associated with spirals (at different radii than corotation) could cause an increase in radial velocity dispersion.

The stability of the simulations has been tested in section 4.4 through multiple runs with varying number of particles, seeds, and durations. Since stochastic variations are possible (Sellwood & Debattista 2009) these checks are necessary. Comparison between three simulations of $N = 10^6$, $N = 2 \cdot 10^6$, and $N = 10^7$ with different seeds but otherwise identical initial conditions showed that despite increasing the number of particles, no discernible difference can be identified. This encourages us to believe that the results are robust against the number of bodies used. It is, however, possible that the difference between the number of bodies in the simulations is not significant enough. Note however that the simulation used in Vera-Ciro et al. (2014) utilised 10^8 particles.

When running a simulation with different seeds but identical initial conditions for 5.5 Gyr instead of 2.2 we found a large number of similarities. Extent in radial migration, importance of particles' vertical motion and the behaviour of top migrators all showed little difference. The top migrators went on to behave in a predictable manner after 2.2 Gyr of evolution. This demonstrates that the results are robust to longer integration timescales.

The last test to simulation stability was trying different random seeds. For this, 5 new simulations were started with different seeds but otherwise identical to the 24 M_d DM halo mass, $Q = 1.5$ simulation from section 4.2. Figure 4.22 shows the slopes of $\sigma_{\Delta L_z}$ against $|v_z|$ at different values of L_z, meaning at different parts of the disc. It is apparent that the variation from one seed to another is not large and unlikely to be the cause of any major discrepancies between them. This, as well as the previous two tests described, are vital tests that increase the robustness of the simulations. The fact that no large differences are observed gives us confidence that the seeds we have used for all test have provided good initial conditions. The outer disc showed some variation which could be due to the smaller number of particles available to the calculation of the standard deviation.

In figures like figure 4.6, when there is little migration present such as in the lower plot, changes in ΔL_z tend to increase with L_z. This is unexpected and appears to contradict results of e.g. Bird et al. (2012). They also tend to stay the same in negative and positive ΔL_z. If we have migration, we expect particles in the outer disc to migrate inwards and vice versa. I can provide no reason why migration would be larger in the outer disc and reasonably migration should not occur equally in inward and outward directions in the very inner and outer disc. Perhaps the observed behaviour here stems from something other than churning, as when migration occurs to a larger extent as in the upper plot, the expected behaviour appears.

The two figures 4.16 and 4.17 show two cases that are the extremes of the simulated DM halos. The upper plots in each case has strong spirals which should migrate almost equally at all heights

and the lower plots should migrate only near the midplane of the disc. From this we expect the lower plots to have similar widths for initial and final distributions and the upper plots to have histograms which increase in width. This is the observed behaviour and correpsonds, as stated, to the level of radial migration. The fact that bins with larger J_z have broader widths than those of smaller J_z is explainable by the fact that stars with greater extent in J_z are considered. The investigation into metallicity is a crude one however and ought to be taken with a grain of salt.

An interesting feature is observed in figure 4.20. In this figure and more so in similar ones, a region with larger $\sigma_{\Delta L_z}$ or a 'yellow' region appears in the outer disc. This is similar to the increase in migration with L_z observed in figure 4.6 and could be due to the same cause. In some plots with very strong migration, this region disappears.

In this thesis I have performed an extensive investigation into the nature of radial migration via churning and attempted to increase and expand upon the understanding of this process which has a significant impact upon local observations and must be taken into account. I have provided an understanding of apparent discrepancies in literature and provided a basis for further detailed studies into radial migration in galaxies not strictly similar to the Milky Way.

5.1 Future work

There is ample room for future work and improvement based on the study presented here. A direction in which it would be very interesting to progress this work would be towards being able to compare to observations and perhaps even provide predictions. One existing example of what would be interesting to do is the work done by Kawata et al. (2017). In their paper they 'paint' particles of their N-body simulation with chemicals using a Markov Chain Monte Carlo (MCMC) technique. This allows them to paint their stars at the beginning of the simulation in such a way that the end result comes out looking similar to the MDF of the SN. This is in strong contrast to the results I have presented where the stars are painted at the start of the simulation using results from Hayden et al. (2015). The difference being that Kawata et al. (2017) in effect looks at chemical mixing up until today where I instead look at mixing starting from today.

It would be interesting to try to include the evolution of chemicals during the integration by utilizing models of chemical evolution and star formation to simulate a 'live' galaxy. Without the addition of chemicals in some manner, the ability to make predictions is extremely limited and due to the existing literature and detailed study of the metallicity in the SN it would appear a logical next step.

Studies like Schönrich & Binney (2009) or Schönrich & McMillan (2017) require an analytical description of radial migration. Currently they assume that the extent of radial migration is independent of J_z. In this study it has been shown that this depends on the nature of the spirals. The dependences found in this work could be put into such models.

During the study of the growth of spiral arms in section 4.1 no attempt was made to identify which spiral modes are dominant at which radius. In figures 4.3 and 4.4 the modes are shown as a function of radius and their strength as a function of time for the simulations. Based on results from papers like D'Onghia (2015) we would expect there to be an increase in mode with radius, that further out

in the disc higher mode spirals would be dominant. It is not possible to identify such behaviour in these results. Figures 4.1 and 4.2 might be better used for identification by eye in this case. Figure 4.1 may show an increase from $m = 2$ to $m = 3$ at $t = 1.1$ Gyr. D'Onghia (2015) does however also show an increase in m with lighter discs and heavier halos which is also seen in these results. A new approach with these results could be to try and identify a relationship between mode and radius.

An interesting features have been found which deviate from current understanding of radial migration, namely an increase of ΔL_z with L_z for low-migration simulations (see figure 4.6 and 4.20). Any continuation of this work should strive to find possible explanations for this behaviour.

There are inclusions to the simulations that could be made to improve the simulations and to more closely resemble reality. The option to include a bulge, a 'live' dark matter halo, or other larger parts of the Galaxy as N-body components would improve the simulations and the comparison to the Milky Way.

Acknowledgements

I wish to extend my gratitude to fellow master student Eric Andersson for a thorough and extensive peer-review of this work, to Guido Moyano Loyola for help on general topics in Galactic dynamics, and everyone else who contributed to my realisation of this work.

Bibliography

Agertz, O. & Kravtsov, A. V. 2016, ApJ, 824, 79

Aumer, M. & Binney, J. 2017, MNRAS, 470, 2113

Aumer, M., Binney, J., & Schönrich, R. 2016a, MNRAS, 462, 1697

Aumer, M., Binney, J., & Schönrich, R. 2016b, MNRAS, 459, 3326

Aumer, M., Binney, J., & Schönrich, R. 2017, MNRAS, 470, 3685

Barnes, J. & Hut, P. 1986, Nature, 324, 446

Bensby, T., Feltzing, S., Lundström, I., & Ilyin, I. 2005, A&A, 433, 185

Bensby, T., Feltzing, S., & Oey, M. S. 2014, A&A, 562, A71

Bergemann, M., Ruchti, G., Serenelli, A., et al. 2014, Astronomy & Astrophysics, 565, A89

Binney, J. 2012, MNRAS, 426, 1324

Binney, J. & Tremaine, S. 2008, Galactic Dynamics: Second Edition (Princeton University Press)

Bird, J. C., Kazantzidis, S., & Weinberg, D. H. 2012, MNRAS, 420, 913

Bland-Hawthorn, J. & Gerhard, O. 2016, Annual Review of Astronomy and Astrophysics, 54, 529

Chiappini, C., Matteucci, F., & Gratton, R. 1997, ApJ, 477, 765

de Jong, R. S. 1996, A&A, 313, 377

Dehnen, W. 1999, AJ, 118, 1201

Dehnen, W. 2000, The Astrophysical Journal Letters, 536, L39

Dehnen, W. 2002, Journal of Computational Physics, 179, 27

Dehnen, W. & Binney, J. 1998, Monthly Notices of the Royal Astronomical Society, 294, 429

Dehnen, W. & McLaughlin, D. E. 2005, MNRAS, 363, 1057

Dehnen, W. & Read, J. I. 2011, European Physical Journal Plus, 126, 55

D'Onghia, E. 2015, ApJ, 808, L8

Edvardsson, B., Andersen, J., Gustafsson, B., et al. 1993, Astronomy and Astrophysics, 275, 101

Fuhrmann, K. 2011, Monthly Notices of the Royal Astronomical Society, 414, 2893

Greengard, L. & Rokhlin, V. 1987, Journal of computational physics, 73, 325

Greengard, L. & Rokhlin, V. 1997, Acta numerica, 6, 229

Halle, A., Di Matteo, P., Haywood, M., & Combes, F. 2015, A&A, 578, A58

Hayden, M. R., Bovy, J., Holtzman, J. A., et al. 2015, ApJ, 808, 132

Haywood, M. 2008, Monthly Notices of the Royal Astronomical Society, 388, 1175

Holmberg, J., Nordström, B., & Andersen, J. 2009, A&A, 501, 941

Hurley, J. R., Aarseth, S. J., & Shara, M. M. 2007, ApJ, 665, 707

Kawata, D., Allende Prieto, C., Brook, C. B., et al. 2017, ArXiv e-prints

Larson, R. B. 1974, MNRAS, 169, 229

McMillan, P. J. 2017, MNRAS, 465, 76

McMillan, P. J. & Dehnen, W. 2007, Monthly Notices of the Royal Astronomical Society, 378, 541

Minchev, I., Chiappini, C., & Martig, M. 2014, A&A, 572, A92

Minchev, I., Martig, M., Streich, D., et al. 2015, ApJ, 804, L9

Mustill, A. J., Davies, M. B., & Johansen, A. 2017, MNRAS, 468, 3000

Nordström, B., Mayor, M., Andersen, J., et al. 2004, Astronomy & Astrophysics, 418, 989

O'Brien, D. P., Morbidelli, A., & Levison, H. F. 2006, Icarus, 184, 39

Press, W. H., Teukolsky, S. A., Vetterling, W. T., & Flannery, B. P. 1992, Numerical recipes in C. The art of scientific computing

Reid, M. J. & Brunthaler, A. 2004, ApJ, 616, 872

Roškar, R., Debattista, V. P., Quinn, T. R., Stinson, G. S., & Wadsley, J. 2008a, ApJ, 684, L79

Roškar, R., Debattista, V. P., Quinn, T. R., & Wadsley, J. 2012, MNRAS, 426, 2089

Roškar, R., Debattista, V. P., Stinson, G. S., et al. 2008b, ApJ, 675, L65

Schönrich, R. & Binney, J. 2009, Monthly Notices of the Royal Astronomical Society, 396, 203

Schönrich, R. & McMillan, P. J. 2017, MNRAS, 467, 1154

Searle, L. & Sargent, W. L. 1972, The Astrophysical Journal, 173, 25

Sellwood, J. A. & Binney, J. 2002, Monthly Notices of the Royal Astronomical Society, 336, 785

Sellwood, J. A. & Debattista, V. P. 2009, MNRAS, 398, 1279

Sellwood, J. A. & Valluri, M. 1997, MNRAS, 287, 124

Solway, M., Sellwood, J., & Schönrich, R. 2012, Monthly Notices of the Royal Astronomical Society, 422, 1363

Springel, V. 2005, MNRAS, 364, 1105

Teuben, P. 1995, in Astronomical Data Analysis Software and Systems IV, Vol. 77, 398

Toomre, A. 1964, ApJ, 139, 1217

Vera-Ciro, C., D'Onghia, E., Navarro, J., & Abadi, M. 2014, The Astrophysical Journal, 794, 173

Vila-Costas, M. B. & Edmunds, M. G. 1992, MNRAS, 259, 121

Wadsley, J. W., Stadel, J., & Quinn, T. 2004, NewA, 9, 137

Wielen, R. 1977, A&A, 60, 263

Wielen, R., Fuchs, B., & Dettbarn, C. 1996, A&A, 314, 438

Appendix A

Jacobi integral

When considering a non-axisymmetric potential neither total energy or angular momentum is conserved. But their combination, called the **Jacobi integral**, is. It is necessary for the full description of the churning process and we therefore go through it here.

We will follow the derivations used in chapter 3.3.2 of Binney & Tremaine (2008) closely. We take the example of a non-axisymmetric galaxy which rotates in respect to inertial space. So we have a static potential Φ in a reference frame which rotates steadily at angular velocity $\mathbf{\Omega}_\mathrm{p}$, the **pattern speed**. The velocity in the frame is $\dot{\mathbf{x}}$ which gives us a velocity in the interial frame of $\dot{\mathbf{x}} + \mathbf{\Omega}_\mathrm{p} \times \mathbf{x}$ and thus the Lagrangian

$$\mathcal{L} = \frac{1}{2} \left| \dot{\mathbf{x}} + \mathbf{\Omega}_\mathrm{p} \times \mathbf{x} \right|^2 - \Phi(\mathbf{x}) \tag{A.1}$$

and the momentum

$$\mathbf{p} = \frac{\partial \mathcal{L}}{\partial \dot{\mathbf{x}}} = \dot{\mathbf{x}} + \mathbf{\Omega}_\mathrm{p} \times \mathbf{x}. \tag{A.2}$$

We can then get the Hamiltonian through the equation

$$H = \sum_i \dot{q}_i p_i - \mathcal{L} \tag{A.3}$$

where q_i and p_i are generalised coordinate and momentum respectively. The index is for multiple coordinates. We are using the vector $\mathbf{x}$ and can thus write

$$H_J = \mathbf{p} \cdot \dot{\mathbf{x}} - \mathcal{L}. \tag{A.4}$$

We now replace $\dot{\mathbf{x}}$ using equation (A.2) and $\mathcal{L}$ using equation (A.1).

$$\begin{aligned} H_J &= \mathbf{p} \cdot (\mathbf{p} - \mathbf{\Omega}_\mathrm{p} \times \mathbf{x}) - \frac{1}{2} \left| \dot{\mathbf{x}} + \mathbf{\Omega}_\mathrm{p} \times \mathbf{x} \right|^2 + \Phi \\ &= p^2 - \mathbf{\Omega}_\mathrm{p} (\mathbf{x} \times \mathbf{p}) - \frac{1}{2} p^2 + \Phi \\ &= \frac{1}{2} p^2 + \Phi - \mathbf{\Omega}_\mathrm{p} (\mathbf{x} \times \mathbf{p}), \end{aligned} \tag{A.5}$$

Which utilises that $\mathcal{L} = \frac{1}{2} p^2 - \Phi$ and the identity $\mathbf{A}(\mathbf{B} \times \mathbf{C}) = \mathbf{B}(\mathbf{C} \times \mathbf{A}) = \mathbf{C}(\mathbf{A} \times \mathbf{B})$. In the intertial frame $\mathbf{p}$ is the momentum and then $\mathbf{x} \times \mathbf{p} = \mathbf{L}$, the angular momentum. We also have that $\frac{1}{2} p^2 + \Phi$ is the Hamiltonian for the inertial frame and thus we can write

$$H_J = H - \mathbf{\Omega}_\mathrm{p} \cdot \mathbf{L}. \tag{A.6}$$

This equation has no time dependence since $\Phi(\mathbf{x})$ is constant in the rotating frame, and the derivative $dH_J/dt = \partial H_J / \partial t$ along any orbit vanishes. This means that H_J fits the definition of an integral of motion and we call it the Jacobi integral. We find that in a rotating non-axisymmetric potential such as this H and $\mathbf{L}$ are not conserved while the Jacobi integral is. We can rewrite it using the effective potential $\Phi_\mathrm{eff}(\boldsymbol{x}) \equiv \Phi(\boldsymbol{x}) - \frac{1}{2} |\mathbf{\Omega}_\mathrm{p} \times \mathbf{x}|^2$, starting from equation (A.5),

$$H_J = \frac{1}{2} |\dot{\mathbf{x}}|^2 + \Phi - \frac{1}{2} |\mathbf{\Omega}_\mathrm{p} \times \mathbf{x}|^2 = \frac{1}{2} |\dot{\mathbf{x}}|^2 + \Phi_\mathrm{eff}. \tag{A.7}$$

This is most easily shown replacing the momentum in the middle line of equation (A.5) with equation (A.2). The effective potential is the sum of the gravitational potential and a repulsive centrifugal potential.

Appendix B

Table 1: List of parameters used in the NEMO packages with explanations

Parameter	Explanation
	mkWD99disc
out	Output file
nbody	Number of bodies
nbpero	Number of bodies per orbit
R_d	Scale radius: Surface density = Sig_0*(e^(-R/R_d))
Sig_0	Central surface density, see above
R_sig	Velocity dispersion scale radius, $\sigma \propto$ (e^(-R/R_sig))
Q	Toomre's Q, constant if R_sig=0, else Q(Rsig)
z_d	Vertical scale height
Rmax	Maximum disc radius
eps	Particle smoothing length
seed	Seed for random number generator
q-ran	[T/F] Use quasi- instead of psuedo-random numbers
time	Simulation time of snapshot
ni	No. of interation of disc surface density and velocity dispersion
giveF	[T/F] Give distribution function in aux data
accname	Name of any external acceleration field
accpars	Parameters of external acceleration field
accfile	File required by external acceleration field
	gyrfalcON
In	Input file
out	Output file
eps	Particle softening length
kmax	The longest time step is taken to be tau=2^(-kmax)
step	Primary data output is made every step simulation time units.
tstop	The simulation shall be halted at simulation time=tstop
logstep	Log output is made every logstep blocksteps
give	Specifies which data are given with primary data output
accname	Name of any external acceleration field
accpars	Parameters of external acceleration field
accfile	File required by external acceleration field
	accpars
Rh	Halo scale length
Mh	Halo mass
innerh	Halo inner logarithmic density slope
outerh	Halo outer logarithmic density slope
etah	Halo transition exponent
Rth	Halo truncation radius
Rcoreh	Halo core radius